A COMPARISON OF COASTAL TRAPPED WAVE MODEL WITH VELOCITY OBSERVATIONS IN NORSKE TROUGH, NORTHEAST GREENLAND

by

Sohyun Bae

A thesis submitted to the Faculty of the University of Delaware in partial fulfillment of the requirements for the degree of Master of Science in Ocean Engineering

Summer 2021

A COMPARISON OF COASTAL TRAPPED WAVE MODEL WITH VELOCITY OBSERVATIONS IN NORSKE TROUGH, NORTHEAST GREENLAND

by

Sohyun Bae

Approved: ______________________________

Andreas Muenchow, Ph.D.
Professor in charge of Advisory Committee

Approved: ______________________________

Mark Moline, Ph.D.
Director of School of Marine Science and Policy

Approved: ______________________________

Estella Atekwana, Ph.D.
Dean of the College of Earth, Ocean and Environment

Approved: ______________________________

Louis F. Rossi, Ph.D.
Vice Provost for Graduate and Professional Education and
Dean of the Graduate College

ACKNOWLEDGMENTS

First of all, I would like to express my deepest appreciation to my advisor Dr. Muenchow. His great insight, knowledge, and experience set me in the right direction when it comes to research problem and taught me how to be an independent researcher. Additionally, I would like to thank my committee members Dr. Moffat, Dr. Huq, and Dr.Jo for their invaluable advice on this research.

I would also like to extend my deepest gratitude to my friends in the school. They all got me out of trouble related to study, research, and settlement more than once. Thanks to my roommate, Christy for relieving my stress whenever I had some problems.

Outside the school, I appreciate people who helped me settle down in Newark, especially the pastor and his wife. They worried about my predicament, considering it as their own. In addition to them, thanks to my friends Minju, Gilhwan, Sohyun, Suhwoo, Jaewoo, Seyeon, Hoon, Hye Rin, and so on. They all cared and cheered me from Korea or the United States.

My appreciation also goes out to my family for their encouragement and support all through my studies. I could overcome every hardship with their care and encouragement.

TABLE OF CONTENTS

LIST OF TABLES

LIST OF FIGURES

ABSTRACT

Bottom-intensified flow of warm ocean water leads to basal melting of many Greenland glaciers. I here focus on Norske Trough, a topographic depression that transects the generally 150-m shallow continental shelf of Northeast Greenland where I analyze velocity, temperature, and salinity measured from 2016 to 2017. A year-long mooring record indicates mean currents of about 6 cm/s towards the glaciers. Empirical Orthogonal Functions (EOF) reveal that about 80% of the variance is in the same direction as the mean flow. Currents thus move along the sloping bottom towards the glaciers and are modulated by temporal fluctuations. I identify monthly oscillations that are especially pronounced in winter. A more persistent oscillation at 24 days has an amplitude of about 1 cm/s that I diagnose for topographic Rossby wave dynamics. Horizontal motions at this frequency are almost uniform with depth, however, density stratification is not negligible. Observed Burger numbers B are $\mathcal{O}(1)$ with $B = L_d^2/L^2$, L_d the internal Rossby radius, and L the width of the Norske Trough slope region. Ocean physics thus contain both barotropic and baroclinic elements of Rossby wave theory. Predicted and observed velocity profiles across the slope region agree well enough for a 16 km wide channel, however, the dispersion relation for such channels does not allow for baroclinic Rossby waves with the small vertical current shear I observe at monthly periods. I thus conclude that observations and theory are not entirely consistent and do not support the hypothesis that linear topographic Rossby waves explain velocity variations in Norske Trough unambiguously.

Chapter 1

INTRODUCTION

About 15% of globally rising sea level originates from Greenland's melting glaciers (Shepherd et al. [2012]). Over the last 30 years ice loss from the Greenland Ice Sheet quadrupled from 51±65 Gt yr^{-1} to 211±37 Gt yr^{-1} (Shepherd et al. [2012]). Much of this Greenland melt is caused by warm and salty subsurface waters that melts tidewater glaciers such as Jakobshavn Glacier (Holland et al. [2008]), Helheim Glacier (Straneo et al. [2010]), Petermann Glacier (Johnson et al. [2011]), and Nioghalvfjerdsfjorden Glacier (hearafter, 79N Glacier) (Mayer et al. [2018]). The 79N Glacier constitutes Greenland's largest remaining floating outlet glacier. Basal melting reduces the glacier's thickness by 10.4 ± 3.1 m yr^{-1} (Schaffer et al. [2020]). I here focus on the ocean circulation in a canyon that steers subsurface ocean heat towards this glacier. Hence I extend work by Schaffer et al. [2020] and Münchow et al. [2020] at the glacier front and the canyon 150 km from it, respectively.

Bourke et al. [1987] describe first surveys of the extensive Northeast Greenland continental shelf in 1979 and 1984, respectively. At the time summer ice conditions were favorable for icebreakers to reach coastal waters and the glacier for the first time. Figure 1.1 shows this 200 km wide and 400 km long continental shelf between 76N and 81N latitude. The generally 150 m shallow shelf features a topographic depression that cuts across the entire shelf: the bottom of the 20-100 km wide trough systems extend about 250-450 m below the generally ice-covered sea surface (Wadhams et al. [2011]) and has been surveyed properly only recently by Arndt et al. [2015]. The trough or canyon system separates 100-m shallow Belgica Bank in the south-west as the Norske Trough and in the north-east as the Westwind Trough in the north-east. The deep Atlantic sector of the Arctic Ocean borders our study area in the east (Figure 1.1).

Early expeditions surveyed ocean properties such as temperature and salinity profiles. Bourke et al. [1986] estimated geostrophic velocities and postulated a northward flow in both Norske and Westwind Trough. With additional data from 1984, Bourke et al. [1987] confirmed such geostrophic flow in Norske Trough as did Budéus and Schneider [1995] with data collected in 1993. More specifically, all these authors report warm and saline Atlantic Intermediate Water (AIW) of Atlantic origin below fresh and cold Polar Waters (PW) of Arctic origin in Norske Trough (Bourke et al. [1987], Budéus and Schneider [1995]). Analyzing 1992/93 ocean tracer and property data, Budéus et al. [1997] speculated that deeper waters in the trough system spread independently from the upper water column (Budéus and Schneider [1995]).

Schaffer et al. [2017] found that AIW warmer than 1°C advects heat toward coastal tidewater glaciers, 79NG, via Norske Trough by analyzing all available CTD profiles along the trough system. The heat of Atlantic Waters enters the glacier cavity near the bottom, induces basal melting under the ice tongue of 79NG, and transform denser AIW into ligher albeit cooler and fresher waters that exit the glacier cavity near the surface (Schaffer et al. [2020]). Albedyll et al. [2021] investigated that variability of deep inflow is highly correlated to the NEG continental shelf circulation described by Münchow et al. [2020] who discovered a 10 km wide bottom-intensified jet in Norske Trough. The mean bottom-intensified jet is modified in time by dispersive, baroclinic topographic Rossby waves with 20 day periodicities. The observed oscillations propagated their phase measurably across the slope while wave energy moving along the slope towards the glacier at the group velocity of about 131 km day^{-1}. [Münchow et al. [2020] contains an error in Table-3 where the column labeled C_g for group velocity should read λ for wavelength and vice visa.]

Topographic Rossby waves are sub-inertial oscillations governed by conservation of potential vorticity, e.g., $\frac{f+\zeta}{H}$ where f is Coriolis parameter or planetary vorticity, ζ is relative vorticity, and H is the vertical scale of motion (Gill [2003]). Topographic Rossby waves always propagate their phase with a component that has shallow water to the right (left) in the northern (southern) hemisphere (Gill [2003]). The waves are generally dispersive, that is, their propagation varies with the wave number vector which can have components both along and across the sloping bottom. Dispersive waves propagate their energy with a so-called "group velocity" which differs in magnitude and direction from wave phase velocities. Figure 1.2 shows a typical dispersion relation for topographic Rossby waves in an unstratified ocean with a constant slope (Wåhlin et al. [2016]). It depicts how the frequency of the waves varies as a function of the along-slope component of the wave number vector k. While the along-slope phase velocity $c_p^x = \frac{\omega}{k}$ has always the same sign, the group velocity $c_g^x = \frac{\partial \omega}{\partial k}$ has different signs at small and large k (Figure 1.2).

To include the coastal wall effect, topographic Rossby waves can be separated from baroclinic Kelvin waves (Wang and Mooers [1976]). In the limit of long wave (near to the zero wavenumber), the phase of Topographic Rossby and Kelvin waves propagate their phase along the slope, meaning that the phase and group velocity are in the same direction (Figure 1.2). Kelvin waves move at the same phase speed regardless of wavenumbers. Frequency increases linearly with the wavenumber. In contrast, topographic Rossby waves are dispersive, have a maximum frequency, and group velocity in opposite direction for short and long waves (Wåhlin et al. [2016]). For example, at the maximum frequency, the group velocity of topographic Rossby waves is zero (Wåhlin et al. [2016]). Additionally, the phase speed of Kelvin wave ($c_p = \sqrt{gH}$) is much faster than that of Topographic Rossby waves (Figure 1.2). Furthermore, topographic Rossby waves have both along-slope component, k and across-slope component, l of wavenumber vector (Figure 1.3), while Kelvin waves do not have across slope component, l. Therefore, Topographic Rossby waves are distinguished from Kelvin waves. I will discuss wave properties and dispersion relations in more detail below including those of stratified and bottom-intensified waves (Rhines [1970]).

Wang and Mooers [1976] extended coastal trapped wave theory with a numerical model as they considered the effects of a finite coastal wall, density stratification, and a variable bottom. Following analytical results of Rhines [1970] applicable to a weak or "gentle" bottom slope, Wang and Mooers [1976] used a Burger number

$B = (L_d/L)^2$ to describe how the baroclinic Rossby radius of deformation L_d and offshore length scale L impact stratified wave motions for variable bottom topography and density stratification. Wang and Mooers [1976] revealed that topographic Rossby waves become barotropic shelf waves in the limit of small Burger numbers, that is, $B << 1$.

Wåhlin et al. [2016] present persistent 2-day oscillations in observation from a canyon in the Amundsen Sea off Antarctica. The canyon geometry is similar to Norske Trough, Greenland. They applied barotropic theory, because they find that $B < 0.1$ and explain their observations as a topographic Rossby wave that has almost zero group velocity. In the Amudsen Sea, both analytical (Gill [2003]) and numerical (Brink [2006*a*]) dispersion relations compare favorably to moored ocean current observations and are similar to Figure 1.2.

For large Burger number $B >> 1$, Inall et al. [2015] observed sub-inertial topographic Rossby waves in Kongsfjorden, a broad fjord in Svalbard with moored velocity records and historical CTD profiles. They found that the wavelength and phase speed in the summer during strong stratification ($B \sim 800$) doubled relative to the winter, when stratification was weaker ($B \sim 20$). Far away from a coast, fjord, or glacier, Ku et al. [2020] analyzed data from a single ADCP mooring near the sloping outer continental shelf of the Chukchi Sea off Siberia. They described strong evidence of short baroclinic Rossby waves such as a bottom intensified oscillating flow with a period of 35 hours. They estimated wave properties from a vertical decay scale by fitting the hyperbolic cosine variation of baroclinic Rossby waves (Rhines [1970]) to the horizontal velocity observations (Ku et al. [2020]).

Based on the literature reviews, I hypothesize that the seafloor topography of Norske Trough results in topographic Rossby waves. I here investigate new 2016-17 ocean observations to describe spatial structures that I try to explain as dispersive waves that have properties of barotropic and baroclinic shelf waves. More specifically, I use analytical models by Rhines [1970] and Cushman-Roisin [1994] as well as the numerical coastally-trapped wave model of Brink and Chapman [1987] to compare velocity observations to topographic Rossby wave predictions. I thus test the hypothesis that such waves exist in Norske Trough.

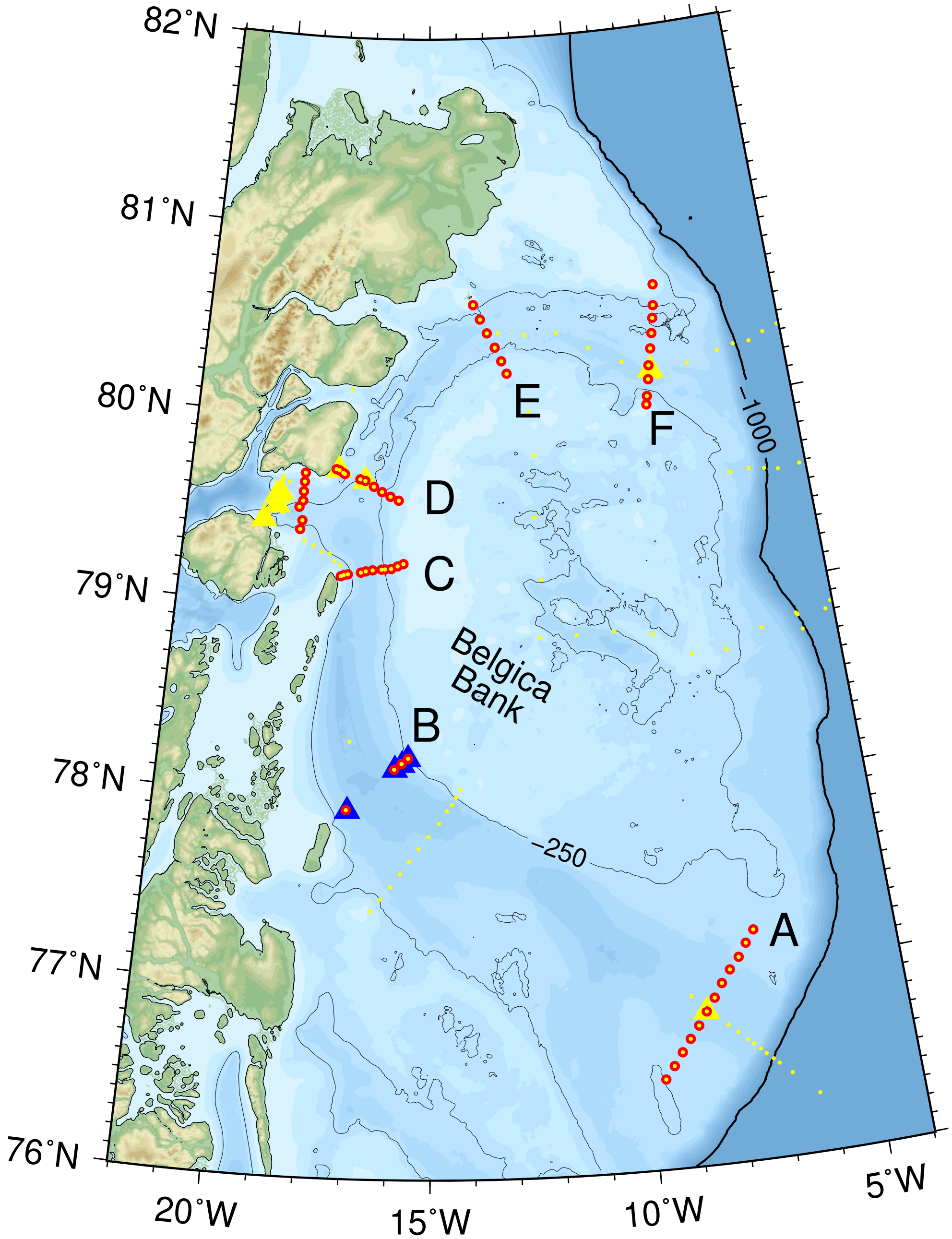

Figure 1.1: Map of Northeast Greenland with 2016-2017 mooring locations (triangles) and 2016 CTD stations (circles). Bathymetry is from Schaffer et al. [2020] with 250 m and 1000 m depth contours outlining the trough system and shelf break, respectively. Data from locations in blue (moorings) and red (CTD) are used in this study while those in yellow are not.

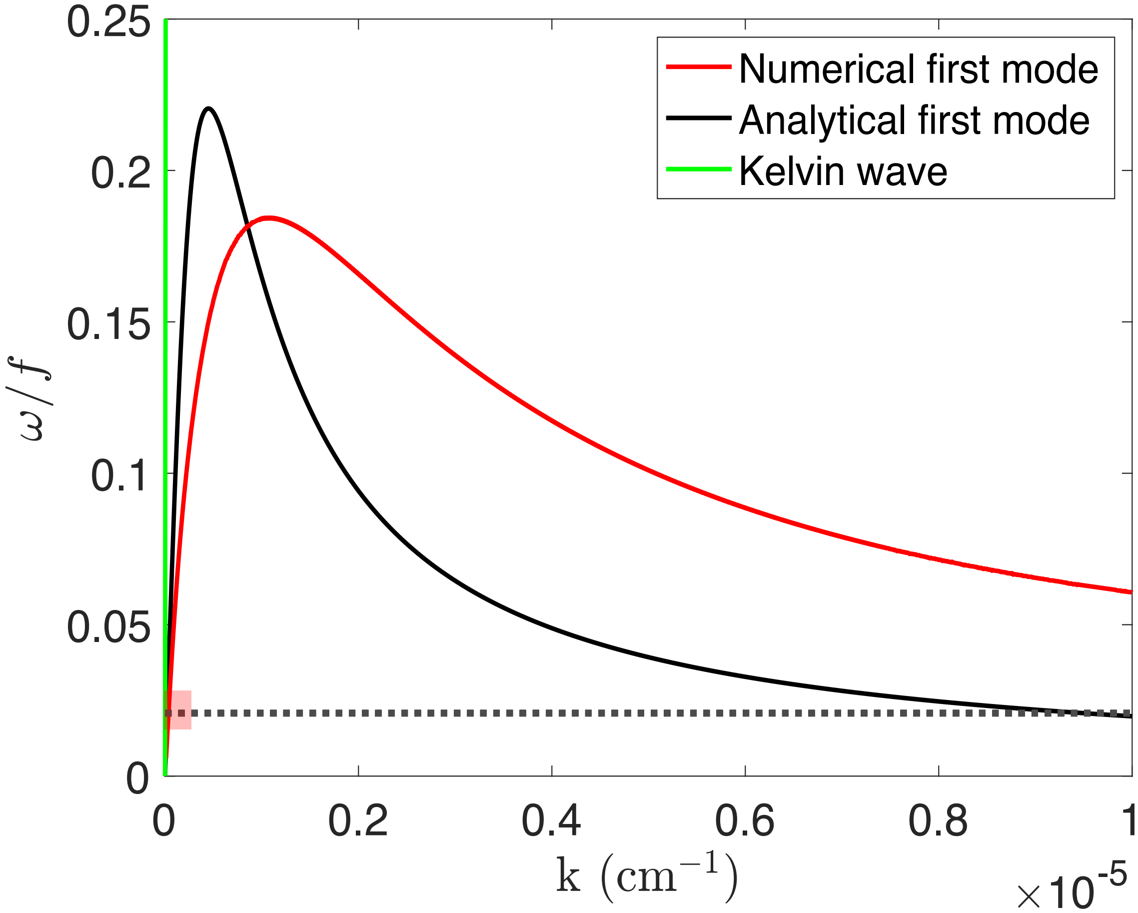

Figure 1.2: Dispersion relation for numerical (red) and analytical (black) solutions for mode 1 based on real and idealized topographies, respectively. Dispersion relation for Kelvin wave (green). Frequency ω is scaled by f which is the Coriolis parameter (0.00014 rad s^{-1}), k is the wavenumber in the along-slope x-direction. The monthly time scale (23-25 days) is indicated by horizontal dotted line below $\omega/f = 0.05$. Shaded red area indicates the corresponding range between the numerical and analytical result with frequency range. To calculate the dispersion relation, I used an channel width L=35km, depth H=514m, and slope α=0.01. Model predictions use the barotropic model and Fortran code described by Brink and Chapman [1987] while analytical results use the formulation described by Wåhlin et al. [2016].

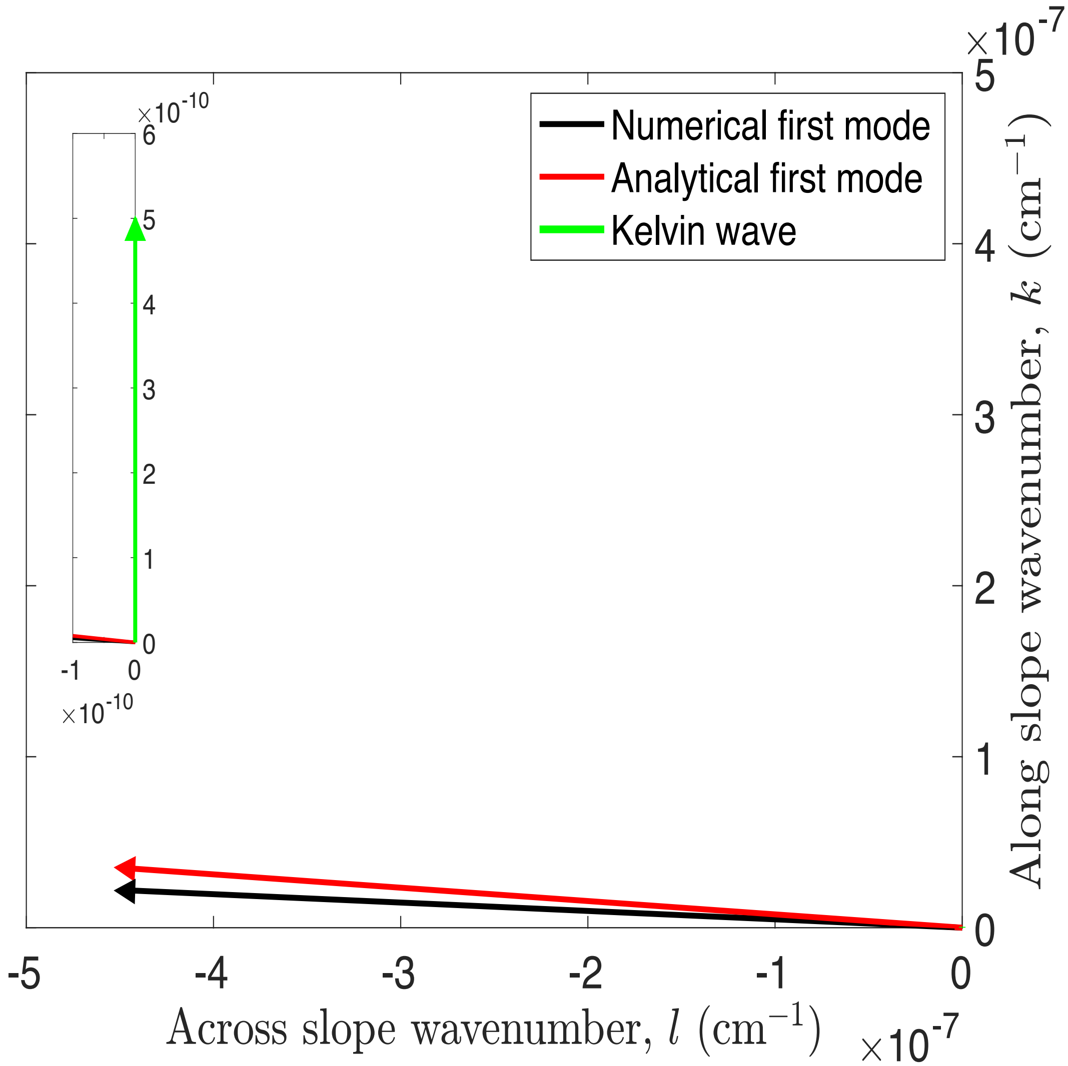

Figure 1.3: Expected phase direction corresponding to the frequency range of the Figure 1.2. Red is analytical result and black is numerical result. k is the corresponding wavenumber in the along-slope x-direction and l is the fixed wavenumber in the across-slope y-direction for mode 1. Green indicates Kelvin wave. Insert figure shows the kelvin wave which is much smaller than topographic Rossby waves.

Chapter 2

DATA AND METHODS

2.1 Data

The observational data presented in this study were collected during a 2016 survey of the German icebreaker and research vessel FS Polarstern. Figure 1.1 shows a map of the continental shelf and slope off North East Greenland, locations of successful 2016/17 mooring deployments, and stations where vertical profiles of ocean properties such as temperature and salinity were measured in August of 2016.

Table 2.1 summarizes mooring details, design configurations, and initial data processing that are identical to those discussed by Muenchow et al. (2020) for a 2014/16 mooring deployment. Three moorings called IDF2, IDF3, and IDF4 are located roughly 5 km apart over the eastern slope of Norske Trough about 40 km to the north where Muenchow et al. (2020) describe data from a similar mooring array using the same acoustic Doppler current profilers (ADCP). The fourth mooring called IDF1 is located on the western side of Norske Trough. IDF1 and IDF3 are taunt-line moorings designed by the Alfred Wegener Institute (AWI) while moorings IDF2 and IDF4 are semi-rigid and anchored to the bottom with a frame that prohibits changes in heading. The University of Delaware (UDel) design was first introduced by Muenchow and Melling (2007). The UDel moorings carried one additional sensor to measure temperature and salinity with an SBE37 MicroCat while the AWI design supported many additional sensors attached to a long mooring line. The ADCPs recorded velocity hourly with a vertical resolution of 8 m (UDel) and 4 m (AWI).

Conductivity, temperature, and depth (CTD) measurements were conducted by an SBE 911Plus CTD rosette system that sampled water properties at 24 Hz.

The sensor systems were calibrated a few month before and after its deployment and I processed the data following standard manufacturer's software routines including averages into 1 m vertical bins (Schaffer et al. [2020]).

Sea ice concentration data (SSMI: Daily 25-km Arctic Sea Ice Concentration, Version 1) were obtained from NSIDC (National Snow and Ice Data Center).

2.2 Method

At each of our four mooring locations, I have hourly time series of velocity vectors with east and north components u and v, respectively, that I transform into along- and across slope directions. Following Kundu and Allen [1976], I find the semi-major and semi-minor axes of the vertically averaged (u,v) vector time series with Empirical Orthogonal Function (EOF). Table 2.2 shows the magnitude and orientations of the semi-major axis Rmaj that I define as the local along-slope direction. Based on this result, all data are rotated by the angle of 109° counter-clockwise from true East for a new coordinate system; along-slope velocity (U) and across-slope velocity (V).

Furthermore, I used EOF analysis to extract vertical current variations in a set of mutually uncorrelated vertical patterns and timeseries. More specifically, I decompose the original signals as

$$\Psi(n,t) = \sum_{n=1}^{N} P_i(t)\phi_i(n).$$

Here, $\Psi(n,t)$ is the anomaly of the original signal, whose mean is subtracted from the original signal. $P_i(t)$ is a set of structures in the time dimension called Principal Components (PC's). $\phi_i(n)$ is a set of spatial modes called eigenvector whose n is the bin number that represents depth at each mooring. Before the calculations, I rotated velocity vectors into along-slope (U) and across-slope (V) velocity components. I thus can identify variability among the different depths. This procedure resulted in 46, 70, and 29 time series (n = 46, 70, and 29) from the different depths at IDF2, IDF3, and IDF4, respectively.

I used wavelet analysis to detect the temporal variation of the spectrum, using

Table 2.1: Mooring coordinates locations and configurations. The AWI-ADCPs operated at 153 kHz and collected single-ping data in 4-m vertical bins while the UDel-ADCP operated at 75 kHz and collected data in 8-m vertical bins. The burst-sampled, single-ping AWI-data was averaged into hourly bins prior to the analyses. The UDel moorings were mounted on a semi-rigid frame whose heading was fixed while the AWI moorings could swivel around their mooring line. The (complex) correlation is between the depth-averaged current vectors at tidal frequencies and barotropic tidal predictions by Padman and Erofeeva [2004].

Mooring	Latitude	Longitude	Depth	Configuration	Correlation, r^2	Direction
IDF1	77° 55.62’ N	17° 5.22’ W	365 m	AWI	0.65	43
IDF2	78° 9.02’ N	15° 54.00’ W	416 m	UDel	0.84	35
IDF3	78° 10.59’ N	15° 43.26’ W	351 m	AWI	0.74	14
IDF4	78° 12.45’ N	15° 33.68’ W	266 m	UDel	0.83	-5

the Matlab toolbox of Torrence and Compo [1998]. Fourier transforms are often used to calculate averaged values of amplitude within a specific period. However, if I apply the Fourier transform over the whole period, I cannot get information on intermittent phenomena (Thomson and Emery [2014]) because it reduces the amplitude as a result of average. Short-time Fourier transform (STFT) can be used to find amplitude but short record length (T) increases the resolution in frequency (1/T). Therefore, since the ocean current variance in my research area changes in time, I decided to use Morlet wavelet analysis according to Torrence and Compo [1998].

Furthermore, wave analysis suggests the band-pass cutoffs at 23-33 days and 23-25 days based on the wavelet analysis and see how signal changes with time and when the signal is strong.

Table 2.2: Statistics of Depth-Averaged Currents. The mean is time average while Rmaj is the semi-major axes for low-pass filtered data (cut-off frequency of 1.6 cycles per day corresponds to 15 hours. Angles are counted positive counter-clockwise from true East.

Mooring	Mean, Orientation	Rmaj, Orientation
IdF1	2.9 cm/s at 107 deg.	64 and 35 cm^2/s^2 at 108 deg.
IdF2	5.9 cm/s at 120 deg.	77 and 22 cm^2/s^2 at 110 deg.
IdF3	6.2 cm/s at 122 deg.	76 and 23 cm^2/s^2 at 115 deg.
IdF4	1.7 cm/s at 121 deg.	76 and 23 cm^2/s^2 at 103 deg.

Chapter 3

OBSERVATIONS

Figure 1.1 shows six sections across the trough system that are labeled A through F from south to north. Figure 3.1 depicts the average salinity and potential temperature across each section at each depth to estimate a single representative vertical profile to see how water masses change along the trough. AIW with temperature above 1 °C and PW with temperature below 0 °C are found for all six sections. In T-S space, observed properties of surface water are similar with the range of -1.7-1.0 °C and 32.0-33.0 g/kg. The variations in T-S properties of deeper water is across the density line with the range of over 0°C and over 34.5 g/kg, which is the same range of AIW defined by Bourke et al. [1987]. The maximum temperature of the subsurface water each section decreases along the trough from south to north.

Figure 3.2 describes the topography of section B and potential temperature and salinity distribution. At section B, the channel is 60 km wide where three moorings (IDF2, IDF3, and IDF4) are deployed over its sloping bottom in the east. One mooring (IDF1) is located on the western side of the channel where the bottom slope is the opposite direction. The bottom slope (α) in the East is almost constant with the value of 0.014, while the bottom slope in the West is 0.01. The warmest waters are found below 150 m depth. Potential temperature reaches above 1.5 °C near the bottom. The salinity reaches the maximum close to 35 g/kg near the bottom as well. The salinity distribution is almost levels across the section entire water depth. Figure 3.3a reveals a single vertical profile of potential temperature and salinity at mooing site IDF3. The warm and saline AIW is located under the cold and fresh PW below 150 m in this research area.

Figure 3.3b displays vertical structure of Brunt-Väisälä frequency (N) and Burger number (B, $\frac{N^2\alpha^2}{f^2}$, $N(\sqrt{-\frac{g}{\rho_0}\frac{\partial\rho(z)}{\partial z}})$ is the Brunt-Väisälä frequency, α is the bottom slope, f is the Coriolis parameter listed in Table 2.2) that estimates the relative importance between the density stratification and the shelf geometry (Cushman-Roisin [1994]). Vertical structure of N has the weak maximum value at 57 m depth, and slightly decays as the depth deepens. Similarly, the vertical structure of B has the weak maximum at 57 m depth and has the value less than 1 below 145 m depth. Brink [2006*a*] mentioned if B <<1, the flow tends to be barotropic. However, since B of $\mathcal{O}(1)$ is not small enough to be barotropic, here I assume baroclinic flow. Next, I analyze vertical and lateral structures of velocity.

Figure 3.3c depicts the vertical profiles of time-averaged velocity of the along- and across-slope components U and V at IDF3. While U shows the largest velocity near 270 m depth, the magnitude of V is much smaller compared to U and remains constant of the whole water column. The constant across-slope velocity can also be seen in other vertical profiles (e.g., IDF1, IDF2, and IDF4, not shown).

Figure 3.4 illustrates the time series of depth-averaged current vectors at IDF1, IDF2, IDF3, and IDF4. While the vectors of IDF2, IDF3, and IDF4 tend to direct to the northwest, the vector of IDF1 shows inconsistent flow. The flow of IDF1 is strongest from October to December and weakens in other periods. On the contrary, strongest flows at IDF2, IDF3, and IDF4 are towards the northwest, which occur in December to February with the weaker flows shown in June and July. I thus find that the time series of depth-averaged velocity vectors resemble each other strongly, especially for IDF2 and IDF3. I here focus on along-slope velocity (U) of moorings IDF2, IDF3, and IDF4 and investigate the flow to see if the current flows barotropically or baroclinically.

Figure 3.5 presents current vector time series at seven selected depths of IDF3. The flow at all depths is mostly to the northwest toward the coast and resembles each other. Like the time series of depth-averaged current vector (Figure 3.4), the current vectors are especially strongest in December to February. The year-long measurements

Table 3.1: Observed environmental parameters of the study area, with past value in Münchow et al. [2020].

Symbol	2014/16	2016/17	Explanation
N (s^{-1})	0.005	0.0051	Brunt-Väisälä frequency
f (s^{-1})	0.00014	0.00014	Coriolis parameter
H (m)	400	514	Bottom depth
α	0.06	0.01	Bottom slope
L_d (km)	14	19	Baroclinic Rossby radius of deformation (NH/f)
R_D (km)	447	506	Barotropic Rossby radius of deformation ($\sqrt{gH}/f$)
L (km)	15	35	Horizontal length scale
B	2.3	0.12	Burger Number, ($N^2\alpha^2/f^2$).

reveal that the depth-averaged U is strong during the same period with the maximum velocity of 24, 32, and 21 cm s^{-1} from IDF2, IDF3, and IDF4, respectively (not shown). The time-mean of depth-averaged U is 5, 6, and 1 cm s^{-1} at IDF2, IDF3, and IDF4, respectively, while all of the across-slope velocities are weaker than 1 cm/s (not shown).

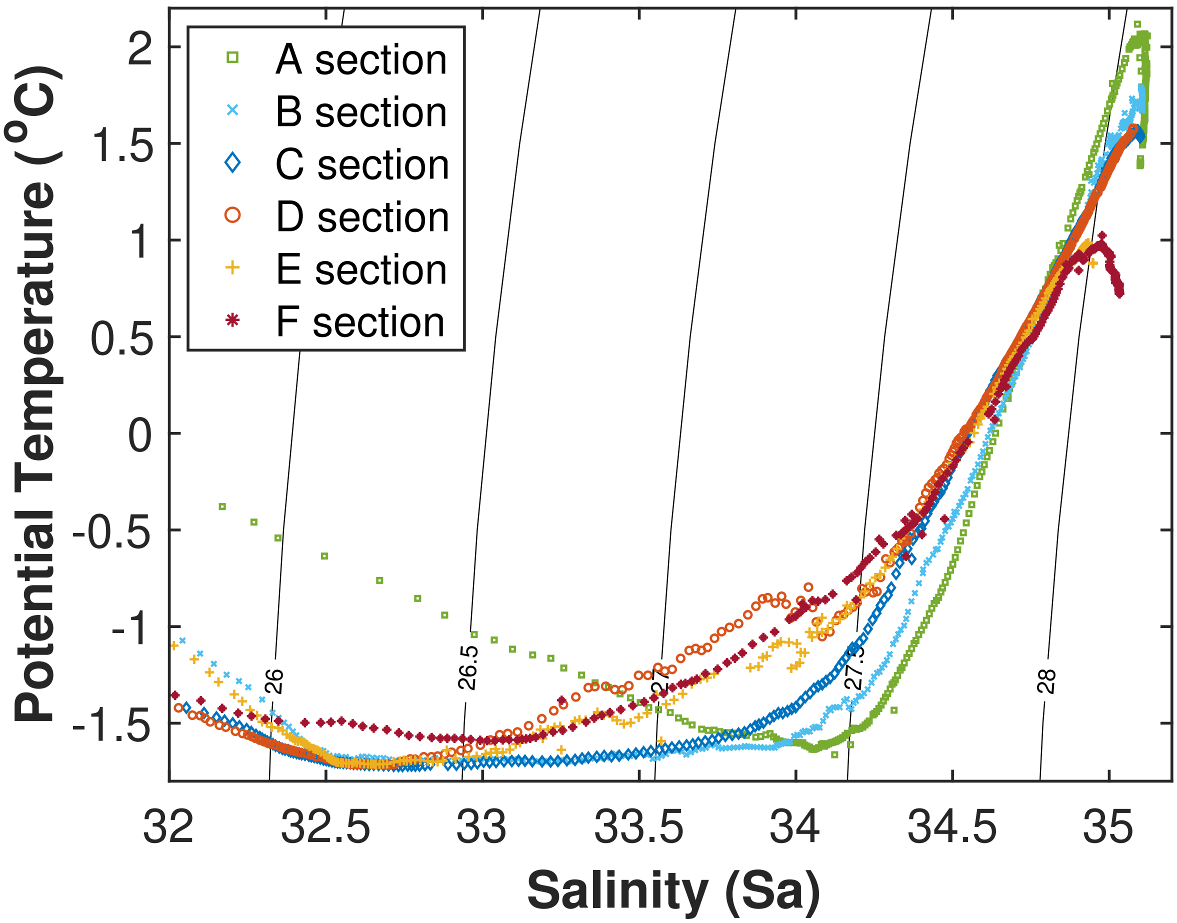

Figure 3.1: Salinity and temperature diagram from 2016 CTD sections A through F that cross the Trough system between latitudes of 76N and 80 N. Data are averaged at each depth for each section whose location is shown in Fig.1.1. Contours indicate density anomaly in kg/m^3. Note the temperature maximum near 2 °C near the 28 kg/m^3 contour that is 2.1 and 1.8 °C on sections A and B, respectively and less than 1.0 °C on section F. Sections C, D, and E near the coastal glaciers have near-bottom temperatures close to that of mooring section B.

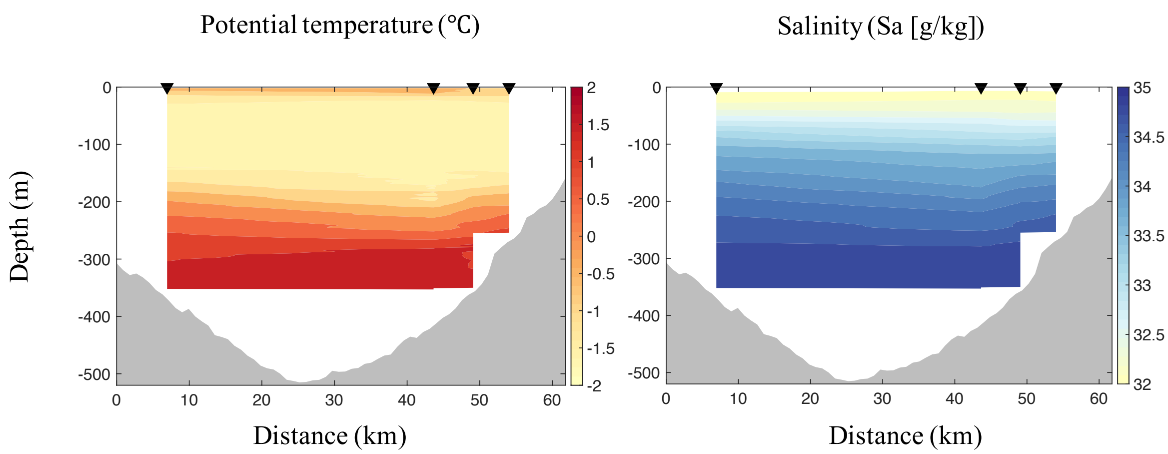

Figure 3.2: Potential temperature and salinity across the mooring sections off Ile de France (Section in B in Figure 1.1) during mooring deployment. Black symbols indicate both CTD and mooring locations. IDF1, IDF2, IDF3, and IDF4 is located from the left. Bottom topography is from 2016 vessel-mounted ADCP surveys.

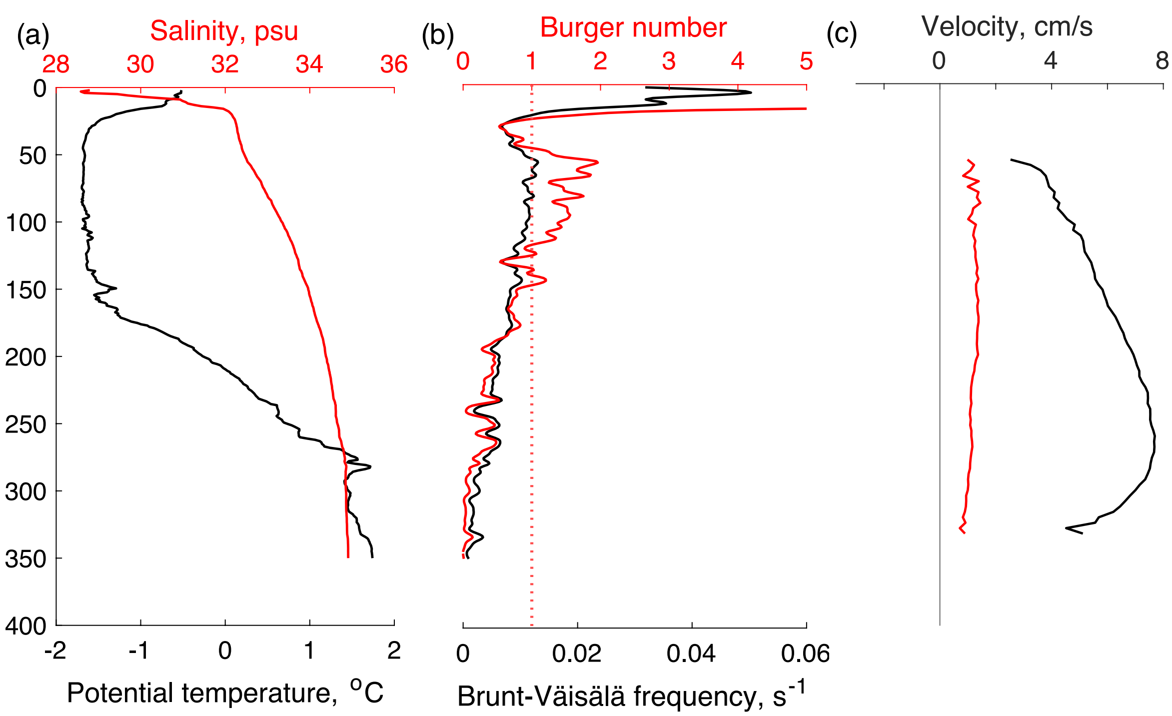

Figure 3.3: (a) Vertical temperature (black) and salinity (red) profile at IdF3 during mooring deployment in August of 2016. (b) Smoothed Brunt-Väisälä frequency (N) (black) and Burger number, $(\frac{N^2\alpha^2}{f^2})$. Note that the Burger number is less than 1 below 150 m. (c) Time-mean velocity component of along-slope (U, black) and across-slope (V, red) at IDF3.

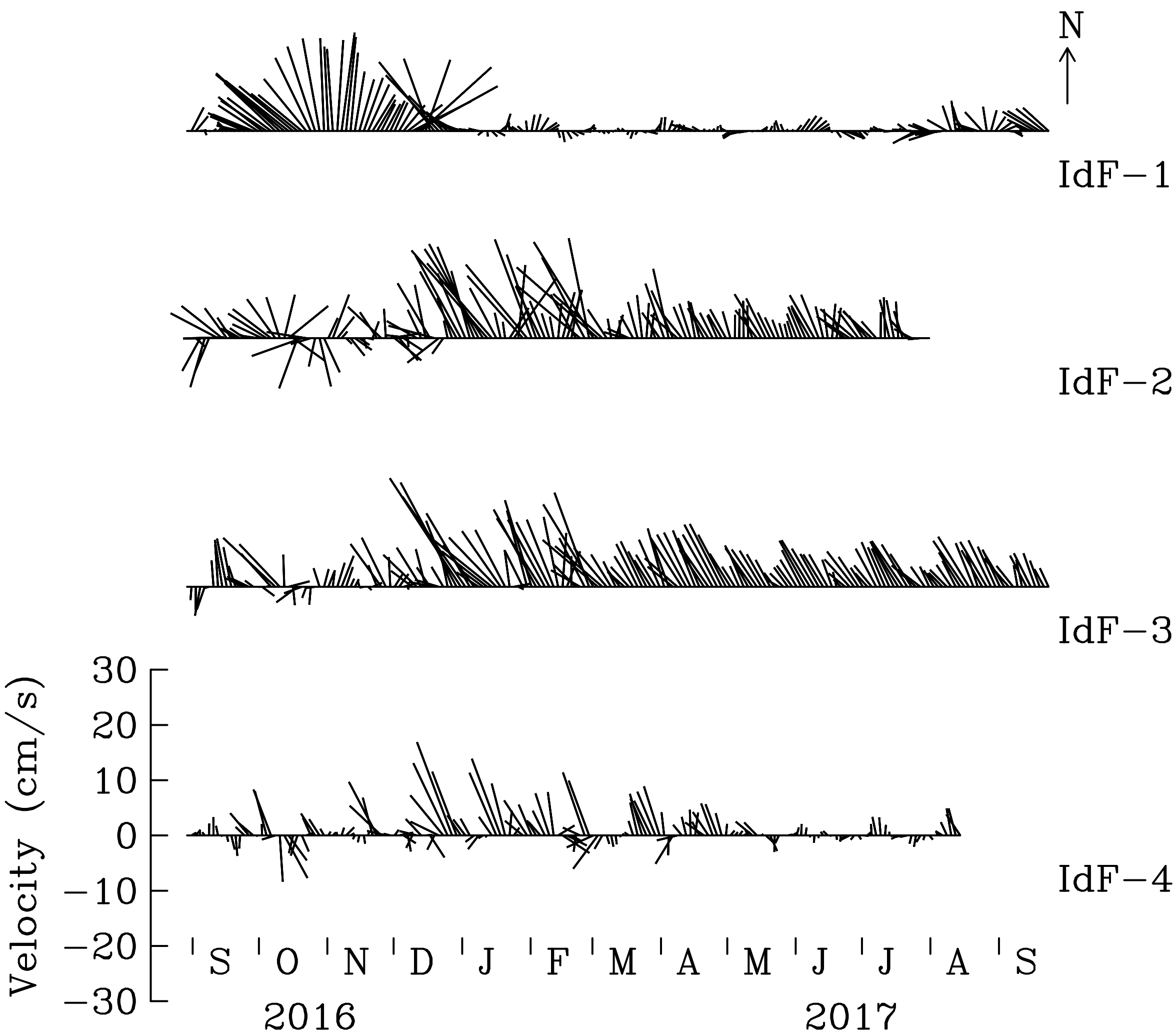

Figure 3.4: Low-pass filtered timeseries of depth-averaged velocity vectors from ADCP moorings across Section B labeled from west to east IdF1, IdF2, IdF3, and IdF4. Locations are shown in Figure 1.1 and Figure 3.2.

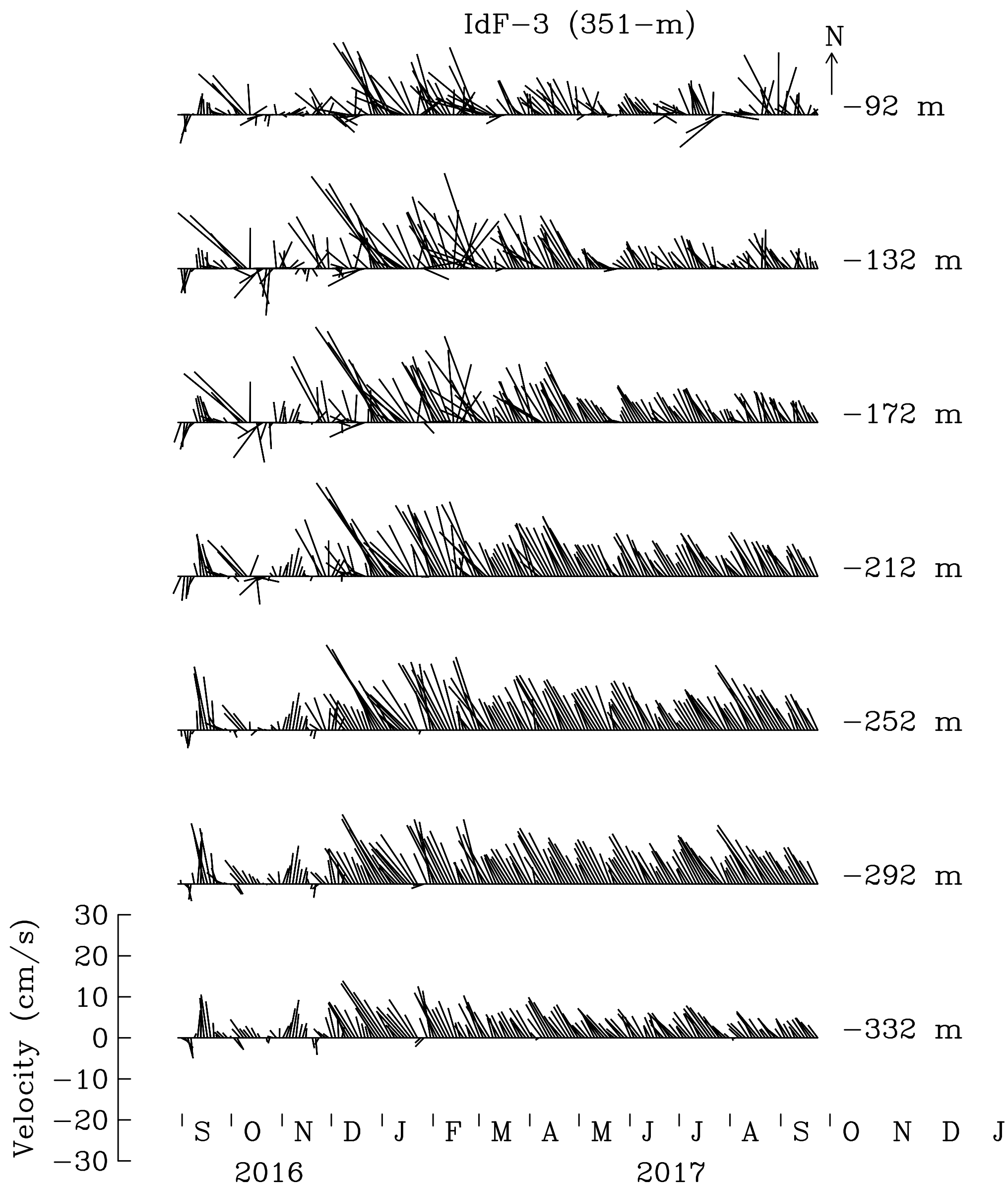

Figure 3.5: Low-pass filtered time series of ocean current vectors at seven selected depths at IDF3. Note the strong vertical correlation of currents to the north-west with an apparent subsurface maximum near 252-m depth. See also Figure 3.3c which is calculated from these data.

Chapter 4

ANALYSIS

I apply both time and frequency domain analyses to the velocity data. The small co-variance in the frequency domain between the western and each of the three eastern moorings justifies my focus on the eastern moorings at IdF2, IdF3, and IdF4. Here I apply time-domain EOF analysis that reveals dominant vertical structures whose temporal modulations correlate strongly with the depth-averaged flow. A frequency-domain wavelet analysis shows how variance at fixed frequencies changes over time during in our observations albeit at broad frequency bandwidth. This poor frequency resolution is overcome by applying a sharp band-pass filter in the time domain to describe velocity oscillations in two different frequency ranges. A final analysis step estimates the amplitude and phase of a single sinusoidal oscillation to the band-pass filtered data with a time domain least-squares data fitting routine. This result will be compared against topographic Rossby wave predictions in the next Chapter-5.

In order to determine the influence of U at IDF1 in relation to U at IDF4, I calculate the coherence square (hereafter, coherence) and phase. Figure 4.1 shows the coherence and phase between the depth-averaged along-slope velocity (U) at IDF1 and IDF4, which are located at the end of the western side of the trough and eastern side of the trough, respectively (Figure 3.2). The coherence reaches almost 0.55 and 0.54 at 0.02 and 0.09 cycles per day (cpd) which corresponds to periods of 50 days and 11 days, respectively. 95% confidence level, however, is 0.52, and the coherence is barely over this value. I thus conclude that IDF1 and IDF4 are not highly correlated with each other, and mainly focus on the IDF2, IDF3, and IDF4 to investigate the eastern side of the trough.

Figure 4.2 represents temporal variabilities and eigenvectors of mode 1 from IDF2, IDF3, and IDF4, using EOF. The variance explained by mode 1 at each station is 72%, 77%, and 80%, respectively. Similar to the depth-averaged current vector, temporal variabilities are also strong in winter (November-February). Furthermore, the temporal variabilities at each station are consistent with the depth-averaged along-slope flow with correlation coefficients larger than 0.99 (not shown). This indicates that vertical fluctuations of velocity are explained by depth-averaged motion. All mode-1 eigenvectors show a peak velocity between 100- and 200- m depth. They all show vertical variations and diminish towards the bottom. Since the most of variance of the temporal variabilities can be explained by depth-averaged motion, I investigate the depth-averaged U to reveal wavelike properties.

To illustrate the temporal variations in the frequency domain, I analyze the wavelet power spectra of the depth-averaged U at IDF1, IDF2, IDF3, and IDF4. The wavelet transformation Figure 4.3 shows the normalized variance as a function of both time and frequency (or time scale labeled "Period"). The peak variance happens at periods 23-33 days, which is present in all moorings except IDF1. The elevated variance are observed especially for winter (November-February), which agrees well with the strong currents in winter described by Münchow et al. [2020].

Figure 4.4 shows the time series of 23-33 days band-pass filtered U. The time series of band-pass filtered data show three periods with different distinct features. From late August to early October, events of enhanced ocean velocities with up to 10 cm/s is present of IDF2, IDF3, and IDF4. From late December to late January, velocity at IDF3 oscillates with the smallest amplitude, while IDF2 and IDF4 are out of phase with similar amplitude, (Figures 4.5 a and b, case 1). In contrast, from late January to late February, velocity at IDF4 alternated slightly around zero, while IDF2 and IDF3 are in phase with the biggest amplitude in IDF2 (Figure 4.4, Figures 4.5 (a) and (c), case 2). The 23-33 days frequency range is broad and likely includes multiple waves. I thus narrow my band-pass filter down to 23-25 days. The data now show a persistent signal in all moorings during the measurement periods (Figure 4.6, case 3).

Especially from August to March, all moorings show in phase oscillations, with the biggest amplitude in IDF3 and the smallest amplitude in IDF4.

Considering the amplitude and phase, I estimate amplitude and phase by fitting observations to the regression, $A(t) = A_0 + A_1 \times \sin(\omega t - \phi)$, where ω represents the estimated frequency, 0.22 radians per day (rad/day) (case 1, 2) and 0.26 rad/day (case 3). A_0 indicates a time-mean flow that for this band-pass filtered data can be considered as an estimate of the uncertainty because the time-mean velocity is zero by filter construction. A_1 indicates the amplitude, and ϕ indicates the phase. The exact values obtained through this method are listed in table 6.1. This result will be compared with numerical result and dealt with in more detail in the chapter-6.

Figure 4.7 and Figure 4.8 shows the coherence and phase between the depth-averaged along-slope velocity (U) at IDF2, IDF3, and IDF4 to calculate the phase of each mooring in more detail. I find that IDF3 and IDF4 has peak around 0.042 - 0.07 cpd (14 - 24 days). The corresponding phase at same frequency range is almost 0 °, indicating that they oscillate in phase. In contrast, the coherence between IDF3 and IDF4 is significant at 14 days frequency. The phase is nearly 53 °, that is, at 0.07 cpd, a phase (53 °) indicates that U at IDF4 leads IDF3 with 50 hours. The phase of 53 ° is shown in frequencies between 0.02 and 0.07. I will discuss more on this in the chapter-8.

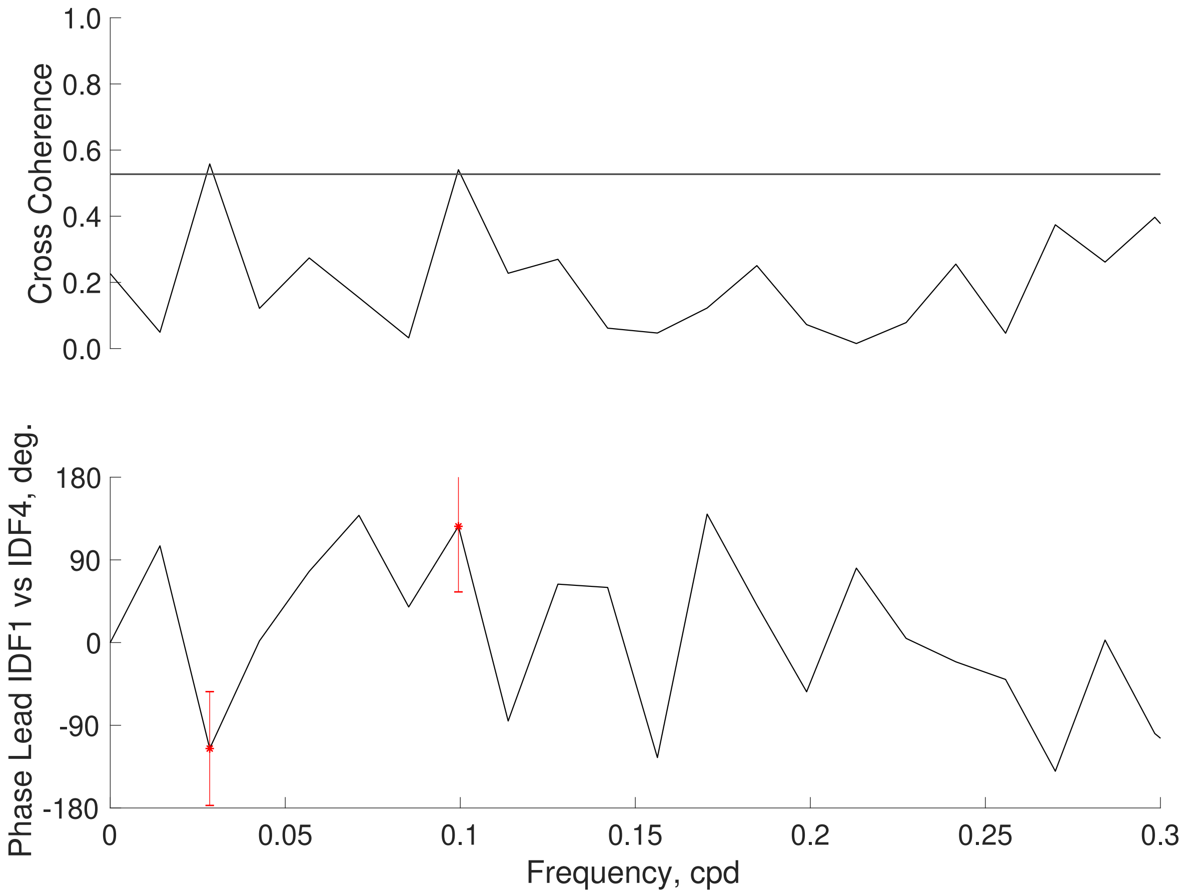

Figure 4.1: (Top) Cross coherence and (Bottom) phase of depth-averaged along slope velocity (U) at IDF1 and IDF4. Black horizontal line indicates the 95 % confidence level. A positive phase means that U at IDF4 leads IDF1, whereas a negative phase means that U at IDF1 leads IDF4.

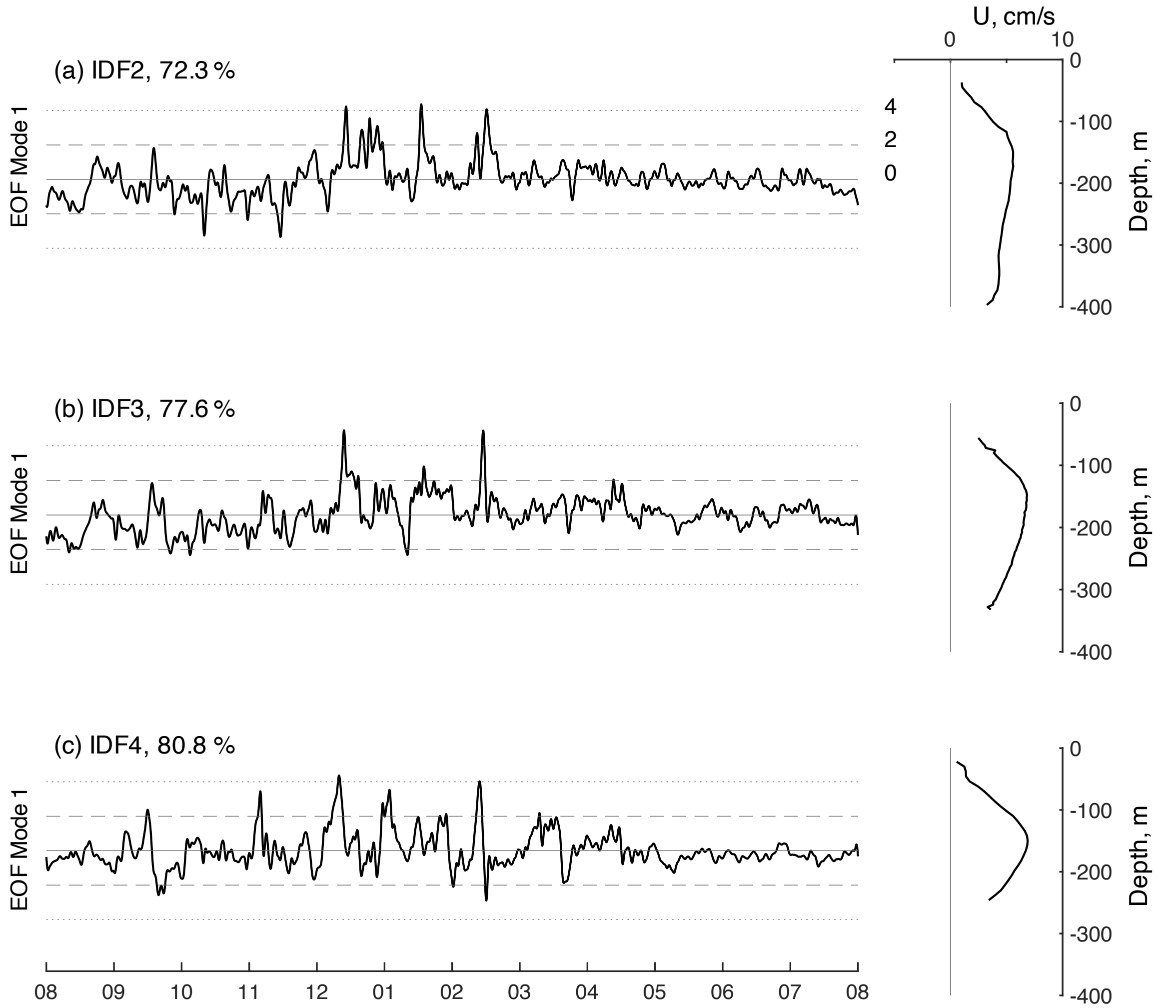

Figure 4.2: First mode of temporal and vertical variability at (a) IDF2, (b) IDF3 and (c) IDF4 organized by empirical orthogonal function (EOF). The variances explained by this statistical mode are listed next to mooring name. Vertical patterns have units of centimeters per second, while time series are non-dimensionalized to have a variance of 1.

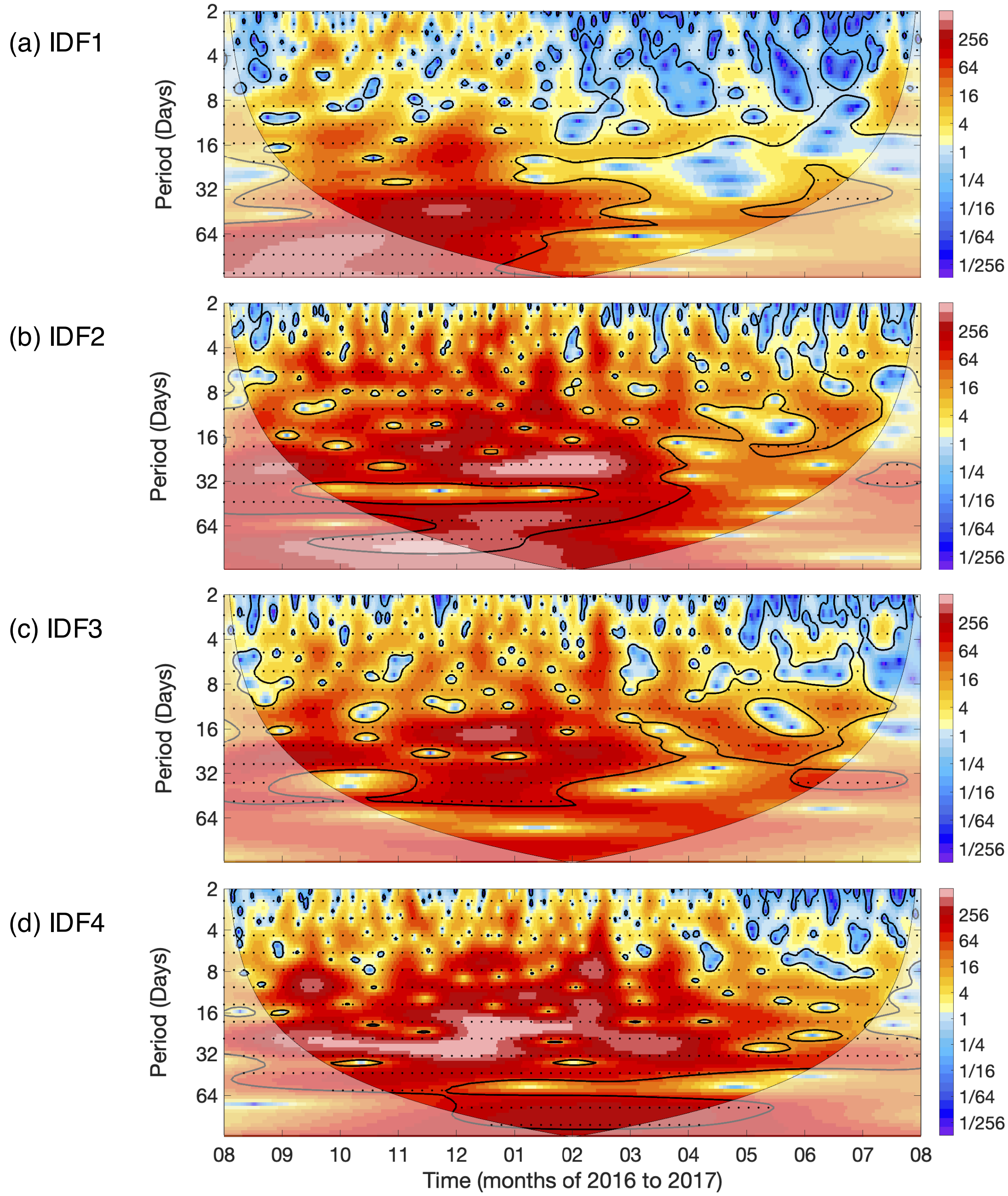

Figure 4.3: Morlet wavelet analysis of vertically averaged U (along-slope velocity) of (a) IDF1, (b) IDF2, (c) IDF3, and (d) IDF4. Opaque regions indicate the "cone of influence" in which edge effects become important. Black contours are 95% significance level. Dotted area indicate over the significance 0.95.

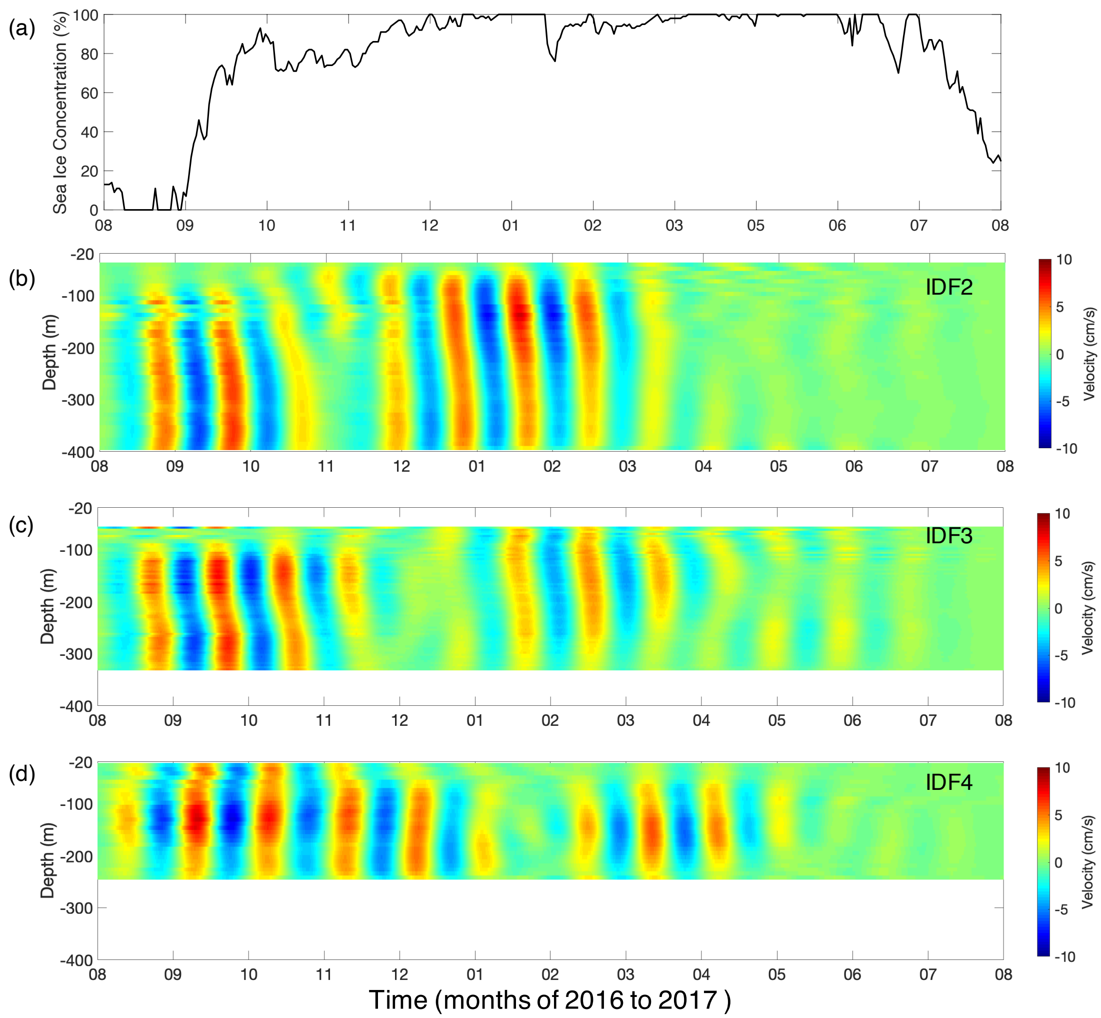

Figure 4.4: Time series of (a) sea ice concentration obtained from National Snow and Ice Data Center. Time series of 23-33 days band-pass filtered U (along slope velocity) from 2016 to 2017 mooring location at (b) IDF2, (c) IDF3 and (d) IDF4.

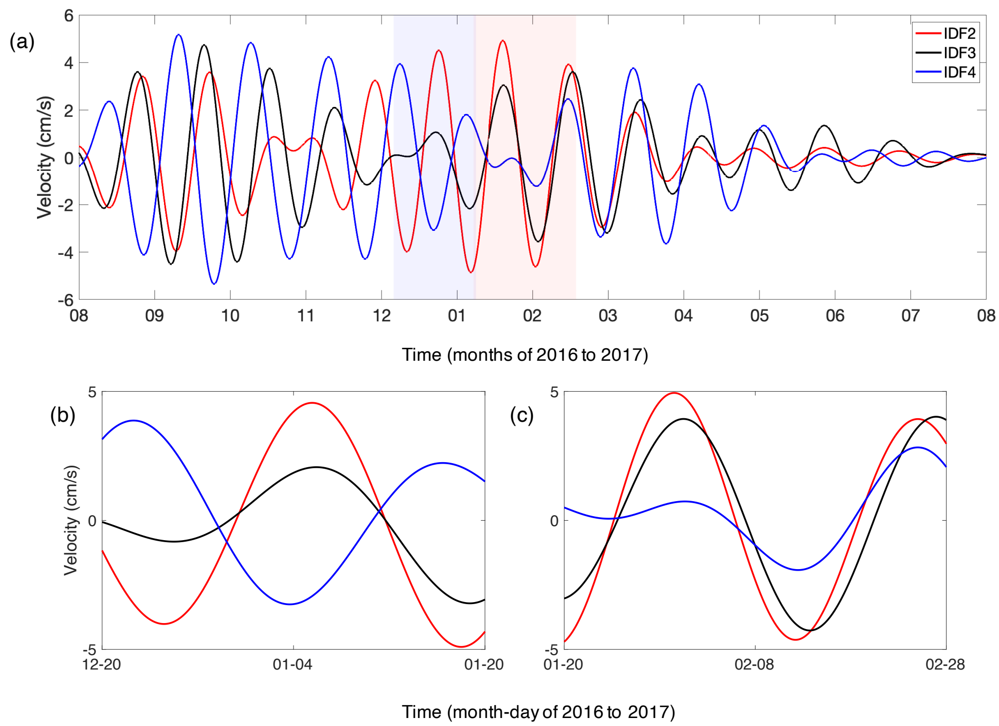

Figure 4.5: Time series of U (IDF2: red, IDF3: black, IDF4: blue) filtered to retain energy in 23-33 days band (a). Blue shaded period corresponds to (b). Red shaded period corresponds to (c).

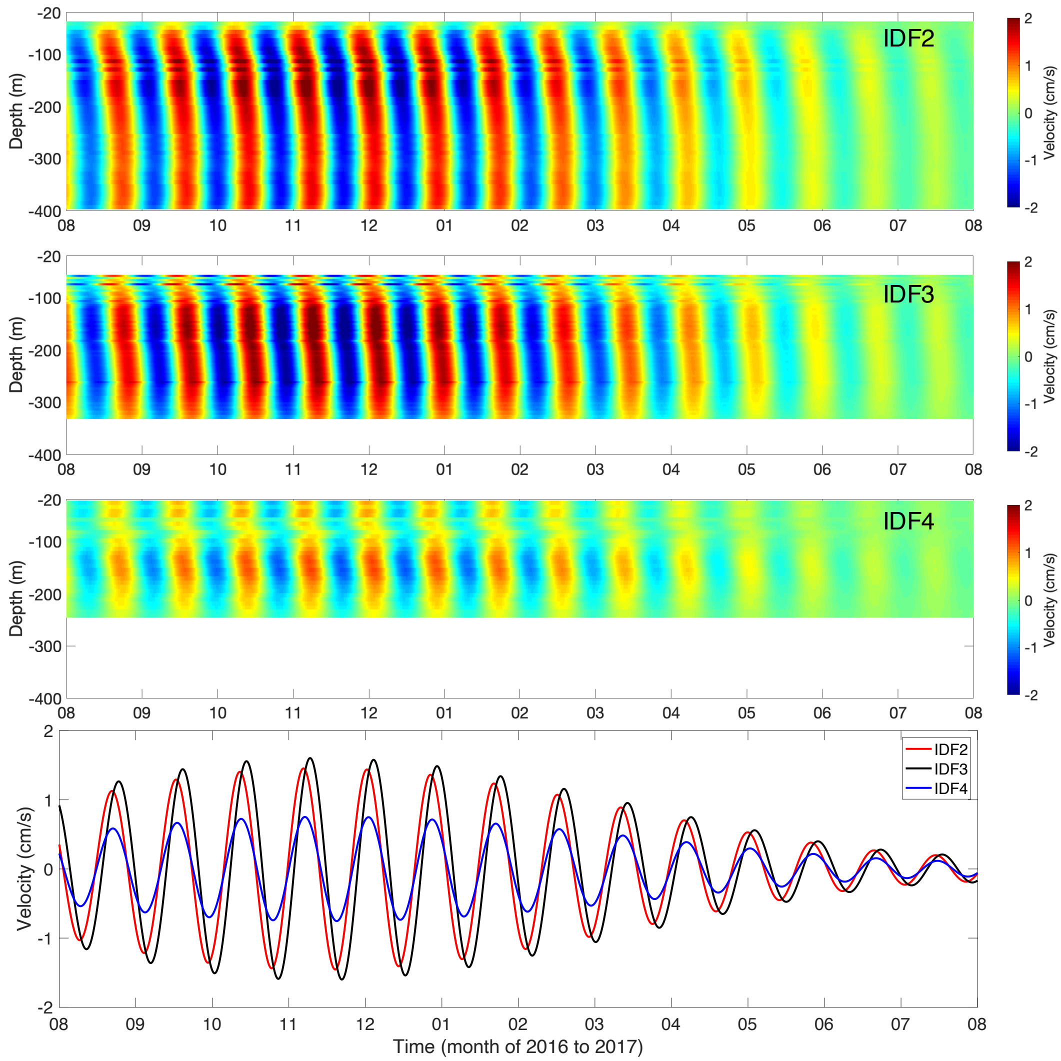

Figure 4.6: Time series of U filtered to retain energy in 23-25 days band. As with Figure 4.5, Red line is IDF2, IDF3 is black, and IDF4 is blue.

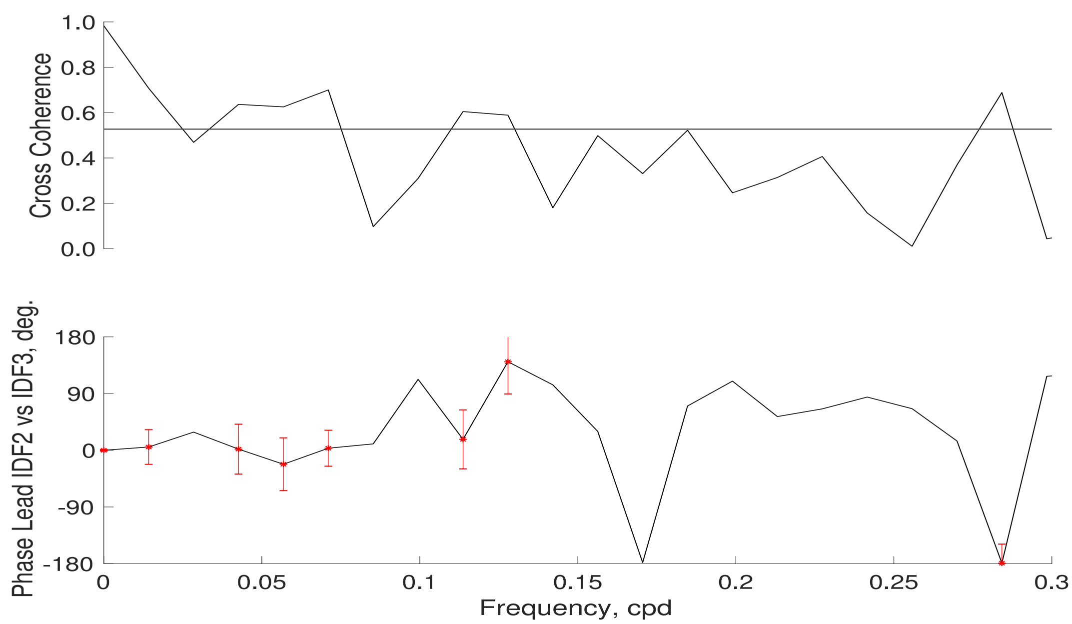

Figure 4.7: (Top) Cross coherence and (Bottom) phase of depth-averaged along slope velocity (U) at IDF2 and IDF3. Black horizontal line denotes the 95 % confidence level for coherency. A positive phase indicates that U at IDF3 leads IDF2, whereas a negative phase indicates that U at IDF2 leads IDF3.

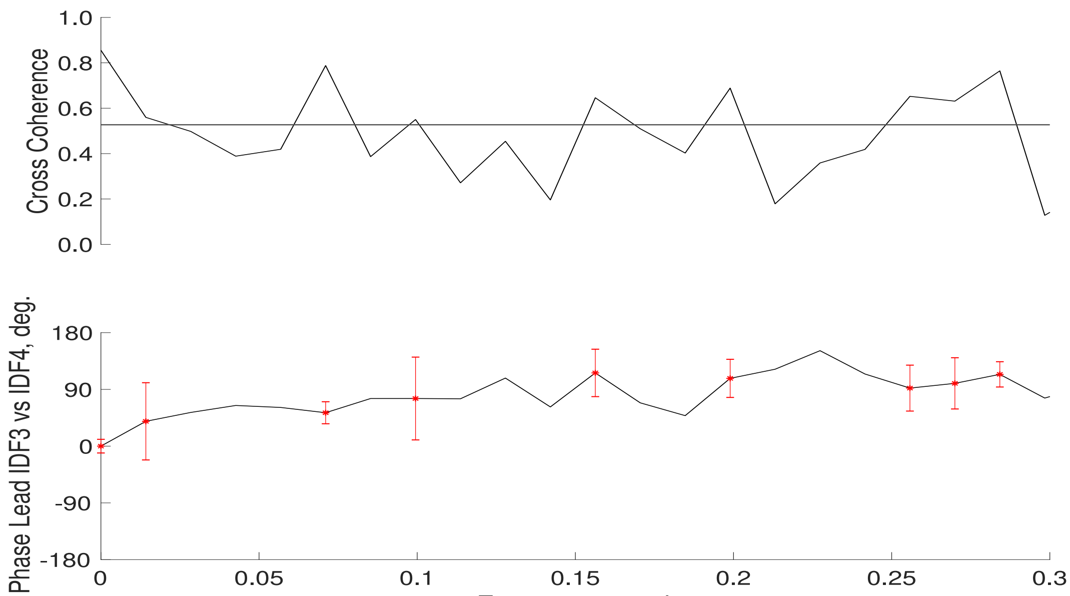

Figure 4.8: (Top) Cross coherence and (Bottom) phase between depth-averaged along slope velocity (U) at IDF2 and IDF3. Black horizontal line specifies the 95 % confidence level for coherency. A positive phase means that U at IDF4 leads IDF3, whereas a negative phase means that U at IDF3 leads IDF4.

Chapter 5

TOPOGRAPHIC ROSSBY WAVE THEORY

The vertical structure of topographic Rossby waves depends on the Burger number that estimates the relative contributions to vortex tube stretching of stratification and a sloping bottom (Rhines [1970]). In the limit of strong stratification and/or large wavenumber (short waves), the flow intensifies near the bottom, because stratification prevents vertical motions induced by the sloping bottom (Rhines [1970], Ku et al. [2020]). As a result of this vertical constraint, horizontal motions and their gradients become large near the bottom. On the other hand, in the limit of weak stratification and/or small wavenumber (long waves), the vertical shear of horizontal currents vanishes, because vertical motions induced by the sloping topography can extend to the surface. The flow then appears barotropic (Rhines [1970], Brink [2006*b*], Wåhlin et al. [2016]).

The dispersion relation of topographic Rossby waves in a stratified channel of width L with a gently sloping bottom was first derived and discussed by Rhines [1970]:

$$\omega = -\alpha N \frac{k}{K_h \, tanh(\mu H_0)}, \tag{5.1}$$

Here $\mu = \frac{N}{f} K_h$ indicates a vertical decay scale and $B = N^2\alpha^2/f^2$ is Burger number. Table 3.1 lists our parameter values for the constant stability or Brunt-Väisälä frequency N, the constant bottom slope α, the constant Coriolis parameter f, and the depth H_0 at a coastal wall. The magnitude of the wave number vector K_h is $\sqrt{k^2 + l^2}$ with components k in the along-slope x and l in across-slope y directions. The decay scale originates from the assumption that vertical variations of baroclinic topographic Rossby waves vary as $cosh(\mu H_0)$

Without considering across-slope boundary conditions Rhines [1970] arbitrarily assigns the same value to the across-slope wavenumber l as to the along-slope wavenumber k, that is, k=l and $K_h = \sqrt{k^2 + l^2} = \sqrt{2}k$. Figure 3 of Rhines [1970] shows the scaled frequency ω/f of waves as a function of the scaled wavenumber $K_h L_d$. For large wavenumbers ($K_h L_d >> 1$) the dispersion curve approach the constant limit $\omega/f = \alpha N/f = \sqrt{B}$. At smaller wave numbers the frequency variations are similar to those of barotropic oscillations whose dispersion is shown in Figure 3 of Rhines [1970] by the dashed line. [I will return to this point farther below in Chapter-6 when I interpret my observations and discuss their somewhat unsatisfactory comparison to this theory.] The insert in Figure 3 of Rhines [1970] exhibits vertical variations of pressure or horizontal velocity fields for three different values of $\sqrt{2}Bk$ (=$L_d K_h$=μH_0=$\frac{NH_0}{f} K_h$ in my notation). I can interpret the square root of Burger number $\sqrt{B} = \frac{NH_0}{fL}$ to measure the baroclinic Rossby radius L_d relative to a geometric length L that is usually related to bottom slope or lateral extend of the channel or width of the continental shelf. This insert figure shows how the vertical variations change depending on the ratio of L_d and L. Strong stratification and/or short wavelength lead to strong bottom trapping. Alternatively, weak stratification and/or long wavelength leads to weak vertical variations and many investigators such as Wåhlin et al. [2016] treat stratified flows with $B << 1$ as barotropic.

Assuming sinusoidal variations across the sloping channel, that is, $sin(n\pi\, y/L)$, Rhines [1970] derives a discrete set of across-slope wave numbers that ensure zero normal velocities at y=0 and y=L of the vertical walls of the gently sloping channel

$$l_n = n\,\frac{\pi}{L}, \tag{5.2}$$

for n=1,2,3, and so on where n indicates the mode number. Other boundary conditions can be applied, too, such vanishing lateral velocity gradients at a distance L from the coast. Wåhlin et al. [2016] applies this latter bounday condition and summarizes analytical results that they applied to a wide canyon off Antarctica

$$l_n = (0.5 + n)\,\frac{\pi}{L}, \tag{5.3}$$

for n=0,1,2, and so on. Here the first mode ($l_0 = 0.5\pi/L$) starts from zero at the coast and has no zero crossing. The second mode has one zero crossing with $l_1 = 1.5(\pi/L)$. Wåhlin et al. [2016] treats the Antarctic topographic Rossby waves as barotropic, because their Burger number $B << 1$. Hence they neglect the effects of stratification and use barotropic wave theory to explain observations from a density-stratified flow. Following Wåhlin et al. [2016], I show in Figure 5.1b how my observed velocity amplitude vary across the slope for modes 1. I discuss these results after I discuss the similarity of dispersion relations for long baroclinic and short barotropic Rossby Waves.

Observations in Figure 4.4 and Figure 4.6 describe velocity variations that vary little with depth. The corresponding vertical decay scale ($\mu = \frac{N}{f} K_h$) thus is small also due to weak stratification and/or small wavenumber in x direction (Figure 3 of Rhines [1970]). Waves in this region are neither short nor long as they generally have $K_h L_d$=O(1). However, B (Burger number) in this paper is not enough small to follow the weak decay (Brink [2006*a*]), so I assume the small wavenumber, K_h. In the limit of small wave number ($K_h L_D$ <<1) which states that the wavelength (λ=$2\pi/K_h, K_h = \sqrt{k^2 + l^2}$) is longer than the internal Rossby radius (L_d, NH/f), and the dispersion relation then reduces to

$$\omega = -\frac{\alpha f}{H}\frac{k}{K_h^2}. \tag{5.4}$$

This dispersion relation is identical to that for barotropic topographic Rossby waves in the limit of short waves, that is, $R_d K_h >> 1$ where $R_d = \sqrt{gH_0}/f$ is the barotropic Rossby radius.

The dispersion relation for linearized, inviscid and homogeneous shallow ocean defined by Wåhlin et al. [2016] or Cushman-Roisin [1994] is

$$\omega = -\frac{\alpha g}{f}\frac{k}{1 + R^2(k^2 + l^2)}, \tag{5.5}$$

In the limit of short wave ($k^2 + l^2 >> 1/R_d^2$), the dispersion relation reduce to equation (5.4).

The modal structure of both long baroclinic and short barotropic shelf waves are independent of stratification and vary little with depth. Furthermore, the modal structure is same for all wavenumbers. Figure 5.1 depicts the modal structures and dispersion curves for long baroclinic and general barotropic shelf wave numerically as determined from the wave model presented in Brink and Chapman [1987]. I used the real topography presented in Figure 5.1 (a) to get the numerical result for the corresponding cross-slope velocity variations for both long baroclinic and short barotropic topographic Rossby waves. The corresponding dispersion waves are shown in Figure 1.2 that I discuss next.

Figure 1.2 shows the numerical and analytical dispersion relation for the first mode. From the dispersion relation, the phase velocity in the direction of wave vector (k,l) with magnitude $K_h = \sqrt{k^2 + l^2}$ is

$$c_p = \frac{\omega}{K_h}. \tag{5.6}$$

Phase velocity always has a component that propagates to the right when facing deeper waters in the Northern Hemisphere and to the left in the Southern Hemisphere.

From the dispersion relation (equation (5.4)), the group velocity in along-slope (x) and across-slope (y) direction is

$$c_x = \frac{\partial \omega}{\partial k} = \frac{\alpha f}{H}\frac{k^2 - l^2}{K_h^4} \tag{5.7}$$

and

$$c_y = \frac{\partial \omega}{\partial l} = \frac{\alpha f}{H}\frac{k^2 + l^2}{K_h^4} \tag{5.8}$$

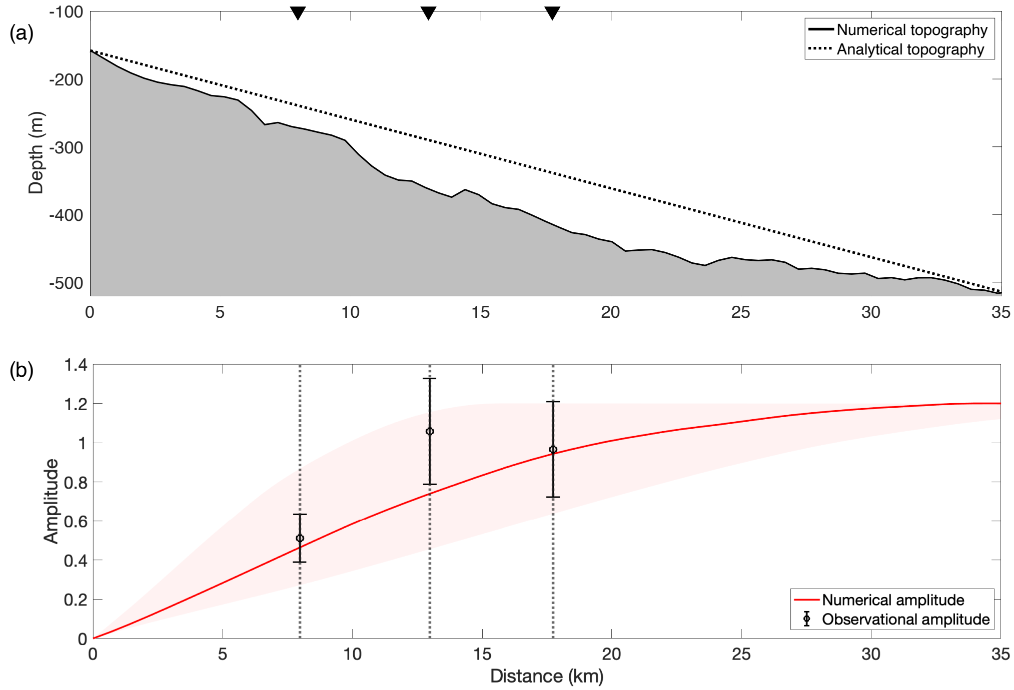

Figure 5.1: (a) Shaded area indicates real topography used for numerical solution and dotted line indicates simplified topography for analytical solution. (b) The normalized mode structure obtained from the numerical solution using codes described by Brink and Chapman [1987]. The mode 1 is shown in red. Vertical dotted lines are the location of moorings IDF2, IDF3 and IDF4 from the left to right. Black circles depict fitted amplitudes (6.1) as mode 1 in 23-25 days frequency for the representative values with the respective standard error (vertical line).

In the long wave limit $K_h * Ld << 1$, the waves become non-dispersive. The phase and group velocities then are equal in magnitude and direction. The energy of long waves then travel with shallow water on the right. When the dispersion reaches its maximal frequency, its slope and thus its group velocity is zero, e.g., ($c_x = \frac{d\omega}{dk} = 0$). The incoming energy then becomes trapped, which Wåhlin et al. [2016] describes as a resonant frequency. For barotropic motions, short waves with $K_h * L_d >> 1$ can propagate their energy with the group velocity in the opposite direction to phase propagation, which means the energy moves in the opposite direction to that of the phase speed.

Chapter 6

A COMPARISON OF ROSSBY WAVE MODEL AND OBSERVATION

In order to prove whether the observed data is topographic Rossby wave, I compare normalized amplitude obtained from the model with estimated observed amplitude. Figure 5.1b shows the modeled along-slope velocity field of near-the-mooring location using the barotropic model of Brink and Chapman [1987]. For mode 1, U increases with the same phase as the depth decreases from inshore to offshore. For mode 2 case, U peaks when it reaches the 500 m depth, and the velocity changes its sign, with a zero crossing between the inshore and offshore (not shown). This indicates that motions inshore and offshore are out of phase for mode 2. To calculate the model sensitivity, I set the channel width as 35 km, while I assume the narrowest channel as 16 km and the widest channel as 55 km.

Observational data indicates three different cases. Within 23-33 days frequency range, case 1 is from late December to late January, and case 2 is from late January to late February (Figure 4.4 and Figure 4.5b). Within 23-25 days frequency range, case 3 is during the measurement periods (Figure 4.6). Here, I focus on case 3.

I calculate the amplitude and phase by regression method presented in table 6.1. Furthermore, I calculate the ensemble average for 14 segments (degree of freedom (dof), 12) to estimate a mean amplitude and its standard error ($\frac{\sigma}{\sqrt{dof}} \times 1.96$ (95% confidence level), σ is standard deviation). Figure 5.1 b shows modeled amplitude and estimated amplitude from observations. This result shows that estimated amplitudes and standard errors are within range of model sensitivity. I thus conclude that the observation and model result fit well, but errors and uncertainties in both model and observations are large.

However, there are some limitations of topography Rossby wave theory to apply in this research area. I next focus on the assumptions and limitations to apply this theory. Topographic Rossby waves are sub-inertial, that is, frequencies ω are always less than f. Wavelet analyses suggest that most variance occurs at monthly time scales for which $\omega << $ f. This satisfies one of the conditions of the theory of Rhines [1970] and use of the dispersion equation (5.1). There are, however, three additional limitations that must be satisfied, if one wishes to apply Rossby wave theory to topographic Rossby waves in a stratified ocean.

First, my research area does not fully satisfy the gentle slope assumption of Rhines [1970] that requires

$$\delta = \frac{\alpha L}{H} << 1, \tag{6.1}$$

where δ is the scaled bottom slope. It measures the fractional change of depth over distance L relative to the total depth H. Note that H/L is not the slope unless δ=1. In this research area, $\delta \sim 0.5$, that is, the slope changes the water depth by a factor of 2 from shallow to deeper water a distance L away. The fractional depth change is $\mathcal{O}(1)$ and violates assumption (6.1).

Second, I assumed with Rhines [1970] and others that the across-slope structure of the topographic Rossby wave varies as $\sin(ly)$ and satisfy boundary conditions in y. This "harmonic" structure function introduces a strong dependence of the results on L of analytical results (Figure 1.2). In contrast, numerically derived dispersion relations allow for more variable across-slope structure- or "eigen-functions" that are not necessarily sinusoidal. This, for example, explains the discrepancy of analytical and numerical results such as shown in Figure 1.2. Furthermore, Cohen et al. [2010] used "Airy function" as structure function for barotropic Rossby wave problems that remove the dependence of the dispersion relation on L.

Third, the observations from Norske Trough do not separate neatly into barotropic or baroclinic classifications. Both density and vertical current shear are weak, but not negligible. My vertical profile of the Burger number in Figure 3.3 indicates B=$\mathcal{O}(1)$ and neither B >>1 nor B<<1 hold. I thus call this the "vague" range. Hence Norske Trough is not entirely barotropic. Therefore, I decided to use the long wave approximation of baroclinic equation Rhines [1970], which gives a dispersion relation identical to that for short barotropic Rossby waves. However, I found that the channel width impacts the dispersion relation via its across-slope wave number, $l_n = \pi/2L$. Figure 6.1 shows general baroclinic dispersion relation equation 5.1 that I overlay with both the short and long wave approximations and how they depend on the channel width L. Long baroclinic topographic Rossby waves do not exist in a channel 16 km wide (if I assume possible narrow channel based on the locations of moorings), because all allowable wave numbers $K_h = \sqrt{k^2 + l_n^2}$ are larger than $1/L_d$ for $l_n = \pi/2L$. Additionally, as the channel width increases, the long wave approximation converges to the general equation and the short wave approximation converges to general equation as they should in the limit of horizontal wave numbers that are much smaller (long waves) and much larger (short waves) than the internal deformation radius L_d. Using the long wave approximation for a channel 32 km wide, I find large discrepancies between the long wave approximation and general equation.

Furthermore, if I assume a wide channel (35 km) in Figure 3.2, both of model and analytical dispersion relation do not exist in the limit of long wave ($K_h * L_d << 1$) (Figure 6.2). This indicates that long baroclinic equation cannot be regarded as short barotropic equation. Also, there might not exist long baroclinic topographic Rossby waves in this 35 km wide channel. Therefore, I cannot apply the barotropic model to research area.

Table 6.1: Calculated amplitude and phase based on observational data using regression method, $A(t) = A_0 + A_1 \times \sin(\omega t - \phi)$, with 28 day frequency and 24 day frequency, ω, respectively.

	23-33 days frequency						23-25 days frequency		
	2016/12/20-2017/01/20			2017/01/20-2017/02/28			2016/08/20-2017/08/06		
	A_0	A_1	ϕ (degree)	A_0	A_1	ϕ (degree)	A_0	A_1	ϕ (degree)
IDF2	-0.25	4.00	227	-0.06	4.29	-49	0.0038	0.91	127
IDF3	-0.03	1.12	267	-0.02	3.32	-53	-0.001	1.00	88
IDF4	0.06	3.02	61	0.02	0.86	-5	0.001	0.48	117

Table 6.2: Expected wave properties based on the analytical equation. Internal Rossby radius of deformation (NH/f) is 19 km. External Rossby radius of deformation (gH/f) is 506 km.

Wave properties	Observations	Analytical model	Numerical model
wavelength (km)	X	120	120
phase speed (km/day)	X	(107, 5)	(82, 6)
group velocity (km/day)	X	117	70

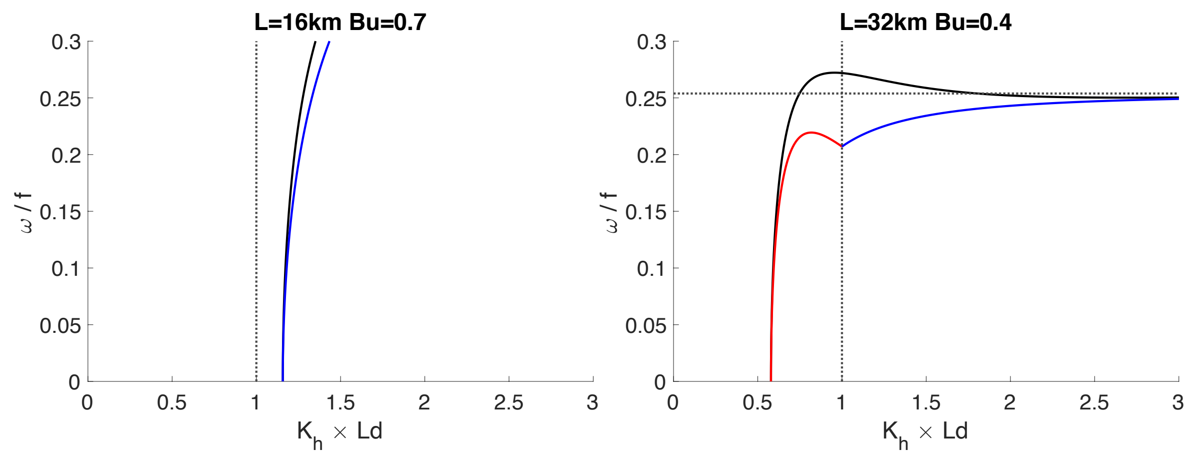

Figure 6.1: Dispersion relation with different channel width (L); general baroclinic wave equation ($\omega = -\alpha N \frac{k}{K_h} coth(\mu H)$, black), long wave approximation ($\omega = -\frac{\alpha f}{H}\frac{k}{K_h^2}$, red), and Short wave approximation ($\omega = -\alpha N \frac{k}{K_h}$, blue). The parameters used in this figure are N= 0.0051 s^{-1}, α=0.01, H=514m, f=1.4×10^{-4}, l=$\frac{pi}{2L}$, $K_h = \sqrt{k^2 + l^2}$. Horizontal dotted line indicates the $\frac{N\alpha}{f}$. Following Rhines [1970], long waves are in the limit of $K_h Ld = NHK_h/f << 1$, and vice versa. These figures show that as the L is large, the general dispersion converges the long wave dispersion at lower wavenumber.

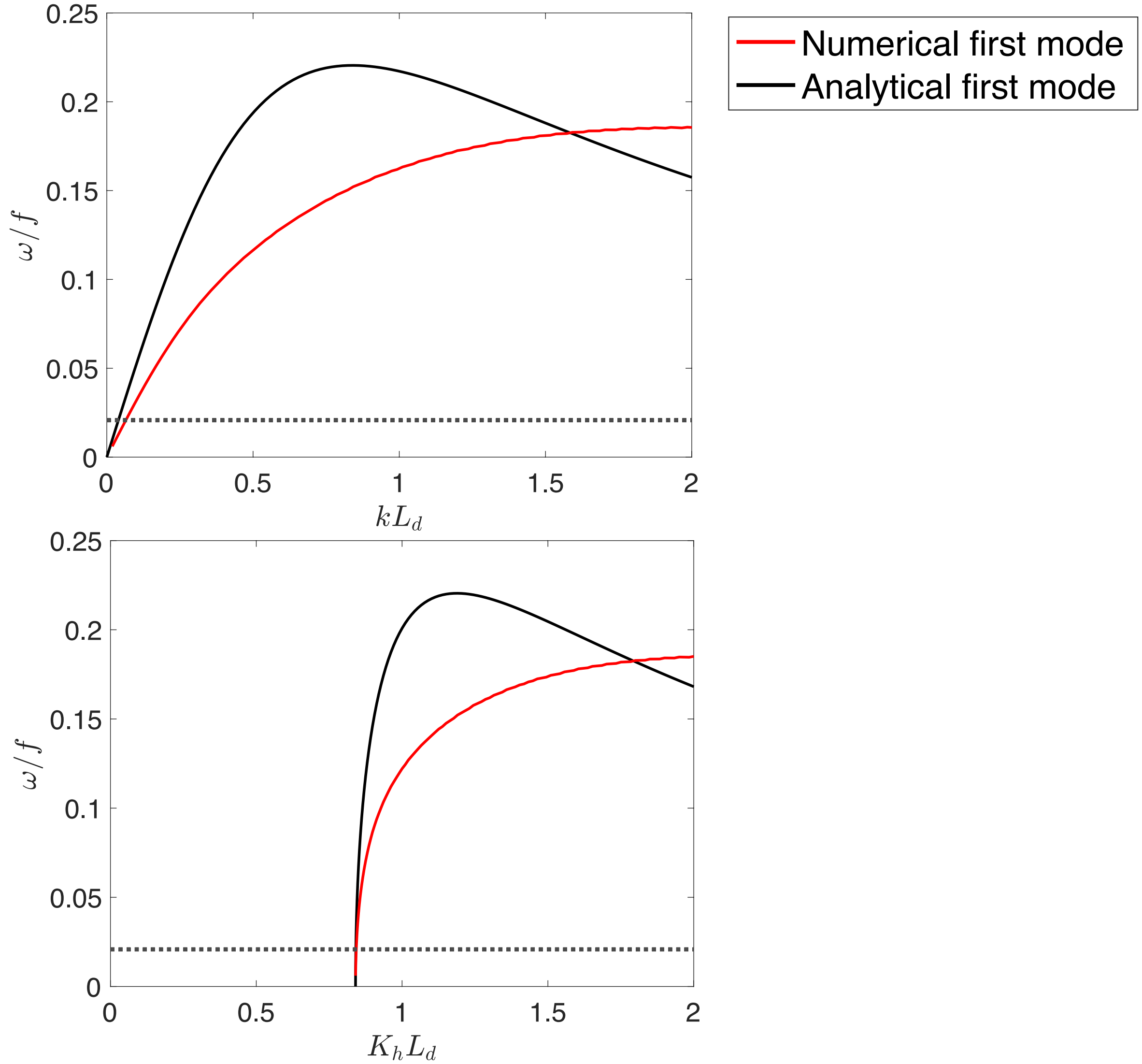

Figure 6.2: Dispersion relation of numerical and analytical model with channel width (L, 35 km). The parameters used in this figure are N= 0.0051 s^{-1}, α=0.01, H=514m, f=1.4×10^{-4}, l=$\frac{pi}{2L}$, $K_h = \sqrt{k^2 + l^2}$. Horizontal dotted line indicates the corresponding frequency range of 23-25 days. Following Rhines [1970], long waves are in the limit of $K_hLd = NHK_h/f << 1$, and vice versa as with Figure 6.1.

Chapter 7

DISCUSSION AND CONCLUSION

I introduce the horizontal current velocity from moorings and CTD data collected within a 60 km wide canyon in Norske Trough, Northeast Greenland. The mooring data describe the flows from Fram Strait offshore to the tidewater glacier, 79NG. I focus on the circulation on one side of the sloping canyon to determine the features of Topographic Rossby Waves.

Subtidal flow is mainly to the northwest towards the coast along the slope, and currents are highly correlated across the slope. EOF mode 1 captured over 72% of the variance at each of three moorings deployed on the same side of Norske Trough. The temporal variability shows a high correlation with the depth-averaged flow which can be interpreted as barotropic motion. However, the vertical profile of Burger number (B) and Brunt-Väisälä frequency (N) is not constant and gave us a "vague" range to consider both barotropic and baroclinic flow.

Wavelet analysis of horizontal velocity, especially along-slope velocity (U) suggests that there is the persistent signal at 23-25 days periods and strong seasonal variations in winter at 23-33 days periods. Horizontal motions at this frequency are uniform with depth, which can be explained by the long baroclinic and/or short barotropic Rossby waves.

The dispersion relation and modal structure of topographic Rossby waves are obtained from the Coastal trapped wave model of Brink and Chapman [1987] to compare the observational data. Predicted and observed velocity profiles across the slope region agree well for a 35 km wide channel. The dispersion relation, however, does not explain the long baroclinic Rossby waves with weak vertical variations. I thus conclude that the observation and analytical evidence does not support the hypothesis that there are linear topographic Rossby waves in Norske trough.

The fact that vague topographic Rossby waves are observed in the present study is surprising, because Münchow et al. [2020] presented similar data from a similar mooring array, but they argued in favor of short baroclinic topographic Rossby waves. Since topographic Rossby waves contain vortex tube stretching due to both stratification and bottom topography (Rhines [1970]), I can explain the different interpretations of data from 2014/16 (Münchow et al. [2020]) and from 2016/17 presented in two ways:

First, sea ice concentrations may have been different in 2014/16 vs. 2016/17. Second, the measurements were made at in different location with different bottom slopes (α), fractional depths (δ), and width (L). As seen in Figure 1.1, the locations of our moorings are only about 24 km away from Münchow et al. [2020] research area and closer to the 79NG. My research area has a more gentle slope ($\alpha = 0.01$) compared with that of Münchow et al. [2020], where α reaches 0.06. These different slopes result in different slope Burger numbers which are about 2.3 in Münchow et al. [2020] and 0.25 for my study, however, both of these are $\mathcal{O}(1)$ as seen in Table 3.1 and the vertical profile of the Burger number B=B(z) in Figure 3.3.

The generation mechanism for the observed topographic Rossby waves also remain unresolved, even though Münchow et al. [2020] identified that Ekman pumping over the shelf break as the forcing of the observed 20-day oscillation. If there are long baroclinic waves in Norske trough, then group velocity is in the same general direction as the phase velocity. This implies that the Topographic Rossby Waves originate from the southeast of mooring sites and that they propagates their phase and group towards the north-west where the coastal glaciers are.

In order to prove topographic Rossby waves in this research area, it is necessary to investigate velocity to estimate phase velocity, wavelength, and group velocity. Figure 1.3 exhibits that phase propagates mostly across-slope, because the value of fixed across-slope wavenumber is larger than that of along-slope wavenumber. I analyze the cross-spectral density to calculate the coherence and phase to find the relation between moorings located across-slope. Unfortunately, there is not a high correlation between all moorings within the frequency range that I got from wavelet analysis. However, there is high correlation between IDF2, IDF3, and IDF4 at 0.07 cpd (14 days) with phase. Therefore, it is imperative to analyze wave properties, assuming that 0.07 cpd is the frequency of topographic Rossby waves as Münchow et al. [2020] did.

Regardless of topographic Rossby waves, persistent oscillations with periods T $\approx$ 24 days exist. The maximum amplitude A_1 of this range is nearly 2 cm/s (1.7 km/day), meaning that current oscillates along the trough with 1.7 km/day. These weak oscillations do not directly impact the 79NG, because they imply particle (or water) excursion of $\Delta x \leq \int_0^{T/2} A_1 sin\frac{2\pi}{T}t\,dt$. This excursion becomes $\Delta x = 12$ km which is small relative to the distance of about 436 km from our mooring location to 79NG. The observed velocity fluctuations then do not impact basal melting of the glaciers, however, the strong mean currents of 5 - 6 cm/s that I observe impact glacier melting.

BIBLIOGRAPHY

Albedyll, L., Schaffer, J. and Kanzow, T. [2021], 'Ocean variability at greenland's largest glacier tongue linked to continental shelf circulation', *Journal of Geophysical Research: Oceans* **126**(5), e2020JC017080. e2020JC017080 2020JC017080.
URL: *https://agupubs.onlinelibrary.wiley.com/doi/abs/10.1029/2020JC017080*

Arndt, J. E., Jokat, W., Dorschel, B., Myklebust, R., Dowdeswell, J. A. and Evans, J. [2015], 'A new bathymetry of the northeast greenland continental shelf: Constraints on glacial and other processes', *Geochemistry, Geophysics, Geosystems* **16**(10), 3733–3753.

Bourke, R. H., Newton, J. L., Paquette, R. G. and Tunnicliffe, M. D. [1987], 'Circulation and water masses of the east greenland shelf', *Journal of Geophysical Research: Oceans* **92**(C7), 6729–6740.

Bourke, R. H., Paquette, R. G. and Weigel, A. M. [1986], Mizlant 85 data report, results of an oceanographic cruise to the greenland sea, september 1985., Technical report, NAVAL POSTGRADUATE SCHOOL MONTEREY CA.

Brink, K. [2006*a*], 'Coastal-trapped waves with finite bottom friction', *Dynamics of Atmospheres and Oceans* **41**(3-4), 172–190.
URL: *https://linkinghub.elsevier.com/retrieve/pii/S0377026506000212*

Brink, K. H. [2006*b*], 'Coastal-trapped waves with finite bottom friction', *Dynamics of Atmospheres and Oceans* **41**(3-4), 172–190.

Brink, K. H. and Chapman, D. C. [1987], *Programs for computing properties of coastal-trapped waves and wind-driven motions over the continental shelf and slope*, Woods Hole Oceanographic Institution.

Budéus, G. and Schneider, W. [1995], 'On the hydrography of the northeast water polynya', *Journal of Geophysical Research: Oceans* **100**(C3), 4287–4299.

Budéus, G., Schneider, W. and Kattner, G. [1997], 'Distribution and exchange of water masses in the northeast water polynya (greenland sea)', *Journal of Marine Systems* **10**(1-4), 123–138.

Cohen, Y., Paldor, N. and Sommeria, J. [2010], 'Laboratory experiments and a non-harmonic theory for topographic rossby waves over a linearly sloping bottom on the f-plane', *J. Fluid Mech* **645**, 479–496.

Cushman-Roisin, B. [1994], *Introduction to Geophysical Fluid Dynamics*, Prentice Hall.
URL: *https://books.google.com/books?id=nL8RAQAAIAAJ*

Gill, A. E. [2003], *Atmosphere-ocean dynamics*, number 30 *in* 'International geophysics series', nachdr. edn, Acad. Press, San Diego. OCLC: 249294465.

Holland, D. M., Thomas, R. H., de Young, B., Ribergaard, M. H. and Lyberth, B. [2008], 'Acceleration of Jakobshavn Isbræ triggered by warm subsurface ocean waters', *Nature Geoscience* **1**(10), 659–664.
URL: *http://www.nature.com/articles/ngeo316*

Inall, M. E., Nilsen, F., Cottier, F. R. and Daae, R. [2015], 'Shelf/fjord exchange driven by coastal-trapped waves in the a rctic', *Journal of Geophysical Research: Oceans* **120**(12), 8283–8303.

Johnson, H. L., Münchow, A., Falkner, K. K. and Melling, H. [2011], 'Ocean circulation and properties in petermann fjord, greenland', *Journal of Geophysical Research: Oceans* **116**(C1).
URL: *https://agupubs.onlinelibrary.wiley.com/doi/abs/10.1029/2010JC006519*

Ku, A., Seung, Y. H., Jeon, C., Choi, Y., Yoshizawa, E., Shimada, K., Cho, K. and Park, J. [2020], 'Observation of Bottom-Trapped Topographic Rossby Waves on the Shelf Break of the Chukchi Sea', *Journal of Geophysical Research: Oceans* **125**(7).
URL: *https://onlinelibrary.wiley.com/doi/abs/10.1029/2019JC015436*

Kundu, P. K. and Allen, J. [1976], 'Some three-dimensional characteristics of low-frequency current fluctuations near the oregon coast', *Journal of Physical Oceanography* **6**(2), 181–199.

Mayer, C., Schaffer, J., Hattermann, T., Floricioiu, D., Krieger, L., Dodd, P. A., Kanzow, T., Licciulli, C. and Schannwell, C. [2018], 'Large ice loss variability at nioghalvfjerdsfjorden glacier, northeast-greenland', *Nature communications* **9**(1), 1–11.

Münchow, A., Schaffer, J. and Kanzow, T. [2020], 'Ocean Circulation Connecting Fram Strait to Glaciers off Northeast Greenland: Mean Flows, Topographic Rossby Waves, and Their Forcing', *Journal of Physical Oceanography* **50**(2), 509–530.
URL: *http://journals.ametsoc.org/doi/10.1175/JPO-D-19-0085.1*

Padman, L. and Erofeeva, S. [2004], 'A barotropic inverse tidal model for the arctic ocean', *Geophysical Research Letters* **31**(2).

Rhines, P. [1970], 'Edge-, bottom-, and rossby waves in a rotating stratified fluid', *Geophysical and Astrophysical Fluid Dynamics* **1**(3-4), 273–302.

Schaffer, J., Kanzow, T., von Appen, W.-J., von Albedyll, L., Arndt, J. E. and Roberts, D. H. [2020], 'Bathymetry constrains ocean heat supply to Greenland's largest glacier tongue', *Nature Geoscience* **13**(3), 227–231.
URL: *http://www.nature.com/articles/s41561-019-0529-x*

Schaffer, J., von Appen, W.-J., Dodd, P. A., Hofstede, C., Mayer, C., de Steur, L. and Kanzow, T. [2017], 'Warm water pathways toward Nioghalvfjerdsfjorden Glacier, Northeast Greenland: WARM WATER PATHWAYS TOWARD 79NG', *Journal of Geophysical Research: Oceans* **122**(5), 4004–4020.
URL: *http://doi.wiley.com/10.1002/2016JC012462*

Shepherd, A., Ivins, E. R., Geruo, A., Barletta, V. R., Bentley, M. J., Bettadpur, S., Briggs, K. H., Bromwich, D. H., Forsberg, R., Galin, N. et al. [2012], 'A reconciled estimate of ice-sheet mass balance', *Science* **338**(6111), 1183–1189.

Straneo, F., Hamilton, G. S., Sutherland, D. A., Stearns, L. A., Davidson, F., Hammill, M. O., Stenson, G. B. and Rosing-Asvid, A. [2010], 'Rapid circulation of warm subtropical waters in a major glacial fjord in east greenland', *Nature Geoscience* **3**(3), 182–186.

Thomson, R. E. and Emery, W. J. [2014], *Data analysis methods in physical oceanography*, Newnes.

Torrence, C. and Compo, G. P. [1998], 'A practical guide to wavelet analysis', *Bulletin of the American Meteorological society* **79**(1), 61–78.

Wadhams, P., Hughes, N. and Rodrigues, J. [2011], 'Arctic sea ice thickness characteristics in winter 2004 and 2007 from submarine sonar transects', *Journal of Geophysical Research: Oceans* **116**(C8).

Wang, D.-P. and Mooers, C. N. [1976], 'Coastal-trapped waves in a continuously stratified ocean', *Journal of Physical Oceanography* **6**(6), 853–863.

Wåhlin, A. K., Kalén, O., Assmann, K. M., Darelius, E., Ha, H. K., Kim, T. W. and Lee, S. H. [2016], 'Subinertial Oscillations on the Amundsen Sea Shelf, Antarctica', *Journal of Physical Oceanography* **46**(9), 2573–2582.
URL: *https://journals.ametsoc.org/jpo/article/46/9/2573/12589/Subinertial-Oscillations-on-the-Amundsen-Sea-Shelf*